Solid Freeform Fabrication 2023: Proceedings of the 34th Annual International Solid Freeform Fabrication Symposium – An Additive Manufacturing Conference
Reviewed Paper

EFFECTIVENESS OF EX-SITU HEAT TREATMENT OF L-PBF AM 17-4PH STAINLESS STEEL SPECIMENS INTENTIONALLY EXPOSED TO DIFFERENT AS-BUILT THERMAL HISTORIES

C. R. Hasbrouck [1,*], Joseph Bartolai [2], Darren C. Pagan [3], and Simon W. Miller [2]

[1] Department of Industrial and Manufacturing Engineering
[2] Applied Research Laboratory
[3] Department of Materials Science and Engineering
The Pennsylvania State University, University Park, PA 16802

Abstract

The presented research demonstrates the effectiveness of H900 heat treatment in eliminating microstructural and mechanical property differences between additively manufactured 17-4PH stainless steel samples of varying thermal histories. For this effort, 17-4PH stainless steel was manufactured using laser-based powder bed fusion on an EOS M280 machine in two geometries: ASTM Standard E8 subsize rectangular tensile specimen geometry with thicknesses of 2mm and 6mm. Thermal histories were manipulated by adding secondary laser passes on each layer at varying levels of reduced power. All samples were heat treated after the build following H900 procedures. Mechanical performance was evaluated with uniaxial quasi-static tensile testing and Vickers microhardness measurements. Metallography was examined qualitatively with optical and electron microscopy as well as quantitatively through electron backscatter diffraction. No statistically significant mechanical property or microstructural differences were discovered, suggesting a successful ex-situ heat treatment.

Keywords: laser powder bed fusion, 17-4PH stainless steel, thermal history, heat treatment

Introduction and Motivation

Since its development in the 1980s, additive manufacturing (AM) has been an exploding area of research due to its ability to build parts in a layer-by-layer fashion based on slices taken from three-dimensional data [1]. This layer-by-layer buildup allows for greater geometric freedom and minimizes material waste when compared to traditional subtractive manufacturing methods such as machining. Additionally, since AM requires no tooling, it allows for expedited, low-cost prototyping when a design needs multiple iterations in a short time frame. AM has more recently gained traction as a popular method for producing metallic parts with complex geometries for critical applications within the aerospace and medical industries [2]. However, all current metallic AM systems use either powder metals, solidification processing, or a combination of both that results in metallurgical differences between AM components and conventional wrought or cast products [2]. Research involving the measurement and mitigation of such AM attributes as mechanical anisotropy, residual stress, and defects is critical for maintaining and predicting the performance of metallic parts produced by AM [3].

[*] Corresponding author: crh33@psu.edu

Of the seven overarching categories of AM, typically only three are used for directly producing metallic components: powder bed fusion (PBF), binder jetting, and directed energy deposition (DED) [1]. Binder jetting is less popular than PBF or DED for critical components due to the need for a post-process infiltration or sintering process. These post-processing steps may lead to localized chemistry and mechanical performance differences, or porosity and dimensional instability, respectively. Both PBF and DED build layers on a solid metal substrate and frequently use either a laser or an electron beam as the energy source for melting the metallic feedstock, typically powder. Electron beams are typically less popular energy sources because they require the build volume to be under vacuum and require magnetic lenses that limit the builds to non-magnetic metals [4]. Both PBF and powder-based DED use powder as the feedstock, but PBF uses a powder bed and DED uses a powder feed [5]. Powder-based DED is popular for additive repair of worn or damaged components, but does not have the level of dimensional control that PBF does [5]. Additionally, DED can use a wire feedstock and a plasma arc power source for faster builds, but sacrifices additional detail and resolution in the process [2]. Therefore, laser-based powder bed fusion (L-PBF) is a popular AM method for producing a wide range of metallic alloys with complex geometries, excellent resolution, and relatively easy-to-manipulate build parameters.

Stainless steels are popular for AM processes due to their combination of good corrosion resistance and achievable mechanical properties. In particular, 17-4PH (AISI 630) stainless steel is a valuable alloy for applications up to 600°F where corrosion resistance and high strength are necessary [6], such as aerospace, nuclear, naval, and chemical industries [7]. AM 17-4PH steel has been compared to its wrought counterparts for development of ex-situ heat treatment practices [6], [8], [9], cyclic deformation and fatigue behavior [7], and stress corrosion cracking [10]. In addition to more typical applications of AM 17-4PH, for example a complex geometry hydraulic manifold [11], AM 17-4PH has also been explored for its high temperature and/or high strain rate performance [12], [13]. AM 17-4PH has been used to produce thin walled parts, where part placement [14] and laser scan length [15] were explored for their effects on resulting microstructure. Additionally, part location [16], build orientation [17], and scan pattern [18] have been explored for their effects on AM 17-4PH fatigue behavior and other mechanical properties, while laser defocusing has been examined for effects on resulting defects and microstructure of AM 17-4PH [19]. In addition to variations in microstructure and mechanical response of 17-4PH produced by AM, its corrosion resistance may be effected by such AM parameters as build bed location [20]. Like many other AM metallic alloys, 17-4PH has been studied with and without hot isostatic pressing post-build [21], and in both as-built and heat treated conditions.

In addition to the intentional manipulation of build parameters for L-PBF, it is important to note that the chemical composition of the feedstock powder can have a significant effect on the as-built microstructure and properties, as well as the post-build heat treatment response of AM 17-4PH [8], [22], [23]. This is most evident for nitrogen-atomized 17-4PH powder that retains enough nitrogen, a strong austenite stabilizer, to greatly increase the amount of retained austenite (RA) during solidification [24]. The alloy 17-4PH is considered a martensitic precipitation hardening stainless steel [25], so any RA remaining in the as-built condition is expected to transform into martensite during heat treatment. If the austenite is stabilized by a high presence of nitrogen, a fully martensitic matrix may not be achieved upon traditional heat treatment regimens [8].

The typical reference for heat treating this alloy in its wrought form is ASTM Standard A564, "Standard Specification for Hot-Rolled and Cold-Finished Age-Hardening Stainless Steel Bars and Shapes," [26]. The highest strength achievable for this alloy occurs at the peak aging condition, designated as H900. Note that the numbers following the initial H in these precipitation hardening thermal cycles indicates the temperature at which the alloy is aged. For example, H900 indicates an aging temperature of 900°F, H1100 indicates an aging temperature of 1100°F, and so on. The heat treatment associated with H900 has two main steps: a solution anneal and an aging cycle. The hold time for each step is typically one hour per inch of material thickness. The purpose of solution annealing is to form a fully austenitic microstructure, which involves raising and holding the temperature of the samples above the austenite start temperature of the alloy, or ~1300°F for 17-4PH [27]. This austenization cycle effectively "erases" any prior thermal history from manufacturing by dissolving the constituent elements [25]. The solution anneal is followed immediately by either an oil (sections up to 3in) or forced air (sections ≥ 3in) quench to room temperature, forming a metastable low-carbon low-strength martensitic microstructure supersaturated with copper [25]. The second step of H900 involves aging the alloy to peak strength by heating and holding the samples at the aging temperature of 900°F, forming copper precipitates that increase ultimate tensile strength to a peak of ~190ksi [25]. The H900 heat treatment has been used in other AM 17-4PH studies [9], [17], [22], [23]. Outside of the H900 peak aging heat treatment, the H1100 [7], [12] and H1150 [22] overaging heat treatments are popular for the AM 17-4PH alloy due to the associated increases in corrosion resistance and fatigue performance over the H900 highest-strength condition. Additional references for heat treatment of 17-4PH that may be used include the ASM Handbook Volume 4D, *Heat Treating of Irons and Steels* [25] and the *ASM Metals Handbook Desk Edition* [28]. Furthermore, some studies have been performed that explore new heat treatment methods for AM 17-4PH outside of conventional wrought standards [6], [8].

While the microstructure of AM 17-4PH has been examined in the literature both as-built and after a number of different thermal cycles, the alloy (whether conventionally or additively manufactured) is nearly always tested for mechanical response after heat treatment to take advantage of the precipitation hardening behavior. Relatively common mechanical property tests used for AM 17-4PH include quasi-static tension testing [8], [12], [16]–[18], compression testing [12], [13], [21], and cyclical fatigue testing [7], [16], [17]. In addition to AM 17-4PH characterization, quasi-static tensile testing is a highly utilized destructive mechanical property test for both fundamental scientific research studies as well as manufacturing process qualifications for most metallic alloy systems in all types of applications, and therefore should be well understood by those who work in manufacturing of metals. The ubiquitous nature of this test is likely not only due to its simplicity, but also because it generates material property data for more than one mechanical response. A single uniaxial tension test can directly measure such material property data as yield strength, ultimate tensile strength, and elongation/ductility [29]. It can also provide indirect calculated estimates of resilience and toughness based on the directly measured properties. An illustration of a typical stress-strain curve from a uniaxial tension test for a ductile material is shown in Figure 1. In addition to the marked strength values, the resilience of the sample is estimated by the area under the stress-strain curve corresponding to the linear elastic region and the toughness is estimated by the area under the entire stress-strain curve.

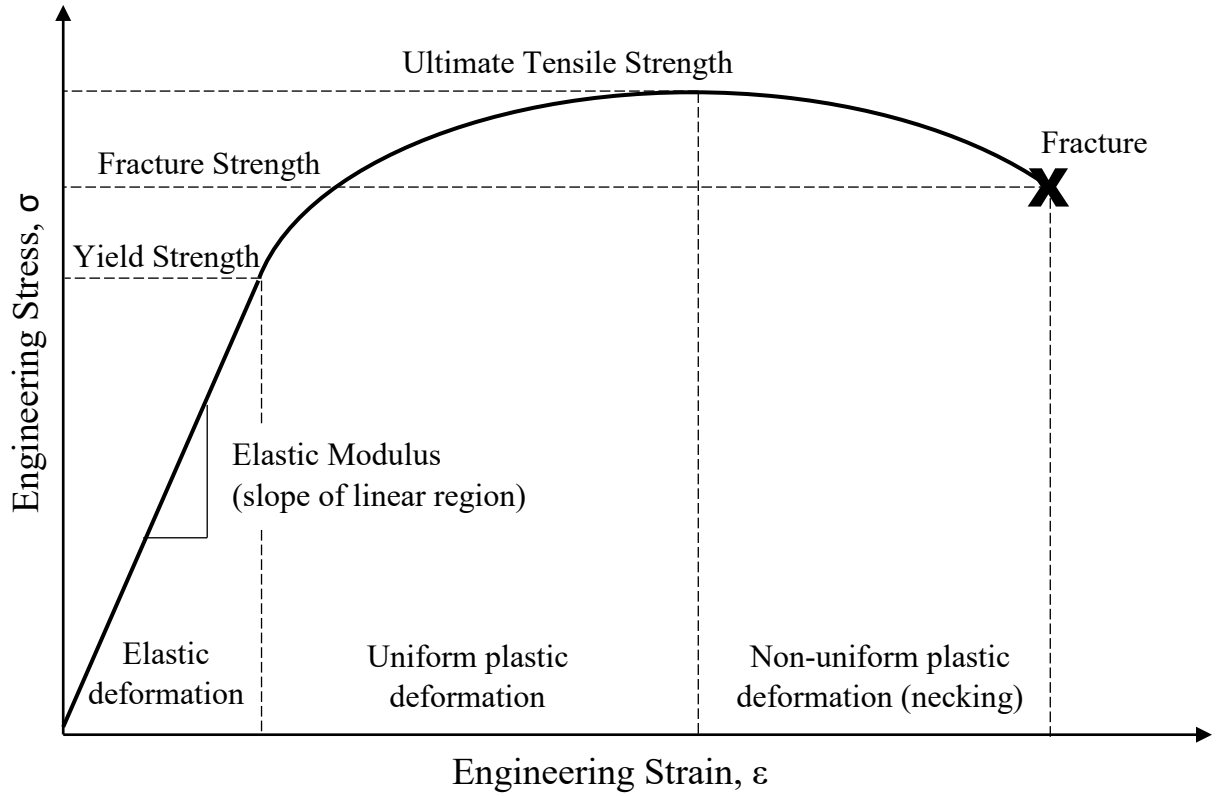

Figure 1: Generic stress-strain curve from a uniaxial tension test of a ductile material.

Because mechanical properties are directly impacted by microstructure, that is also an important consideration when evaluating AM 17-4PH. Popular characterization methods for microstructure include x-ray diffraction (XRD) for phase identification [6], [9], [13], [18], [19], [23], especially when RA is suspected, and electron backscatter diffraction (EBSD) for grain size, morphology, and orientation [7], [9], [10], [14], [15], [17], [21]. Additional characterization methods for AM 17-4PH seen in the literature include microhardness mapping [18] and fracture surface examination [7], [8], [10], [16]–[18] for mechanical response, and optical [6]–[8], [12], [13], [17]–[19], [21], [23], scanning [6], [8]–[10], [15], [19], [21], and transmission electron microscopy [9], [15], [19] for microstructural and chemical composition analysis.

Although mechanical response and microstructural development have been studied extensively in the literature for L-PBF AM 17-4PH samples, the authors believe this is the first research that intentionally modified thermal history of 17-4PH parts by adding additional laser exposures to the material after initial melt and solidification of the feedstock powder. The effectiveness of a standard H900 heat treatment was then verified by mechanical property testing and microstructural characterization. As in the literature, quasi-static tension testing and EBSD were used to analyze mechanical response and microstructure, respectively, after heat treatment. Additionally, microhardness mapping was used to examine local properties, and qualitative metallography was performed by both optical and electron microscopy techniques. The remainder of the paper details the research questions answered by this study; the experimental methodology including: powder distribution and chemistry analysis, machine details and build parameters, heat

treatment procedures, mechanical testing setups, and metallographic procedures; the quantitative data analyses, and the conclusions drawn from this work.

Research Questions

Two research questions (RQ) and an associated hypothesis were developed to understand the effectiveness of ex-situ heat treatment at eliminating microstructural and mechanical response differences of laser-based powder bed fusion (L-PBF) additively manufactured (AM) 17-4PH stainless steel specimens intentionally exposed to different as-built thermal histories:

RQ1: Can a H900 heat treatment effectively standardize the microstructural and mechanical responses of a L-PBF AM 17-4PH stainless steel specimen exposed to a *traditional L-PBF AM as-built thermal history?*

RQ2: Can a H900 heat treatment effectively standardize the microstructural and mechanical responses of a L-PBF AM 17-4PH stainless steel specimen exposed to *additional reduced power laser passes during build?*

Hypothesis: Based on previous research in both AM of 17-4PH stainless steel and more traditional wrought or cast processing, the authors predicted that a H900 heat treatment **will** effectively standardize the microstructural and mechanical responses of L-PBF AM 17-4PH stainless steel specimens intentionally exposed to these different as-built thermal histories.

Experimental Procedures

The experimental procedures will be expanded upon in subsections for each major step of the research, including building the specimens, heat treatment procedures, mechanical testing procedures, and microstructural characterization.

Building the Specimens

The feedstock powder used for this research was AMP 17-4Ar (argon atomized) stainless steel powder supplied by Powder Alloy Corporation (PAC). The composition of this powder follows the chemical specifications of UNS S17400, ASTM A705, and ISO 15156-3 alloy compositions [30]. The specific chemical composition details as measured by NSL Analytical, an ISO17025 approved test laboratory, are detailed in Table 1.

Table 1: Chemical composition of 17-4PH stainless steel feedstock powder.

Element	Spec. Min.	Results	Spec. Max.
Fe	Balance	Balance	Balance
Cr	15.00	15.88	17.00
Ni	3.00	4.24	5.00
Cu	3.00	3.19	5.00
Nb+Ta	0.15	0.25	0.45
C		0.03	0.07
Mn		0.43	1.00
Si		0.74	1.00
S		0.01	0.03
P		0.02	0.04
O		0.1	0.1
N		< 0.1	0.1

Particle size distribution and flow characteristics were measured by both PAC and the Center for Innovative Materials Processing through Direct Digital Deposition (CIMP-3D) at Penn State. PAC measured volumetric particle size distribution using a sieve test according to ASTM Standard B214 [31]. CIMP-3D measured both numeric and volumetric particle size distributions using a TESCAN MIRA high-resolution analytical scanning electron microscope (SEM) utilizing light scattering per ASTM Standard B822 [32]. Both PAC and CIMP-3D measured the Hall flow rate of the powder samples per ASTM Standard B213 [33]. The results of these measurements are detailed in Table 2.

Table 2: Particle analysis results for size distribution and Hall flow rate.

	D10 (µm)	D50 (µm)	D90 (µm)	Hall Flow Average (s/50 g)
PAC (Volumetric)	26.76		54.76	
CIMP-3D (Volumetric)	25.41	38.06	50.33	
CIMP-3D (Numeric)	1.56	3.64	34.97	
PAC				15.7
CIMP-3D				12.05

The large difference in the numeric and volumetric particle size distributions reported is due to the presence of a large number of fine particles. The volume based particle size distribution as measured by CIMP-3D is illustrated in Figure 2.

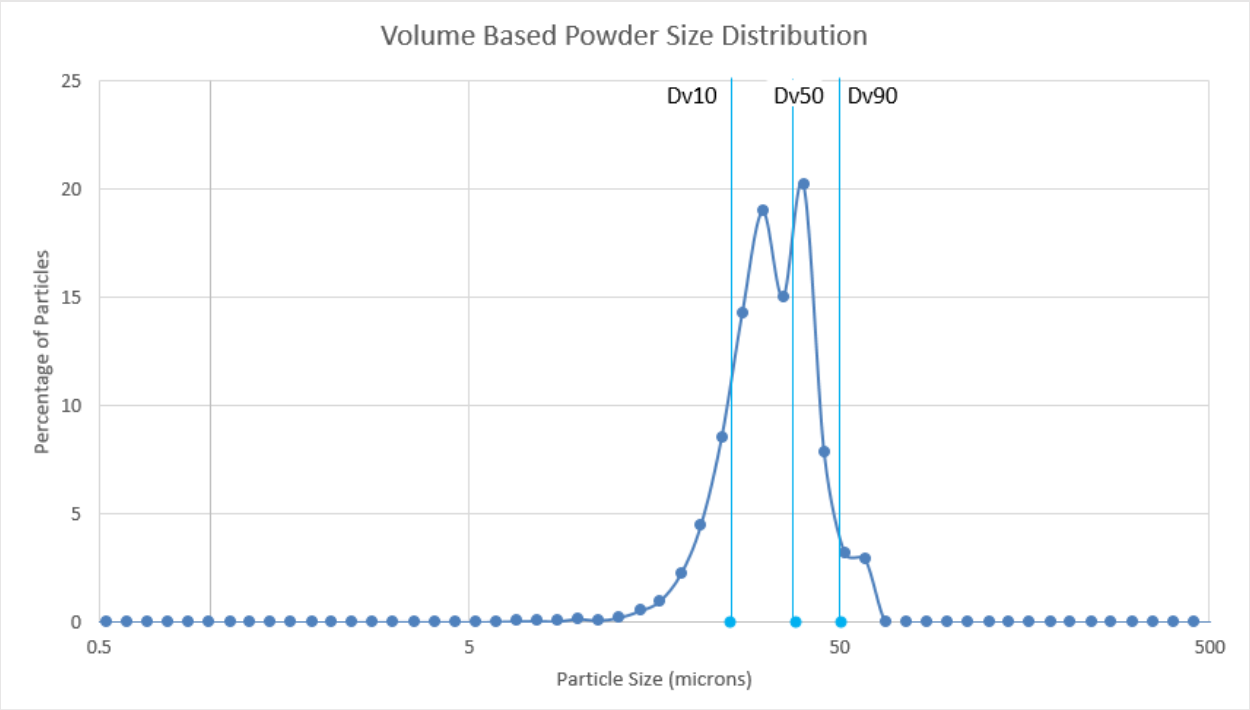

Figure 2: PAC 17-4PH stainless steel volume based particle size distribution.

The presence of fine particles is further illustrated by the SEM images shown in Figure 3. It can be also seen from these images that some of the powder particles experienced collisions with other molten particles during argon atomization and that some particles are extremely lacking in sphericity.

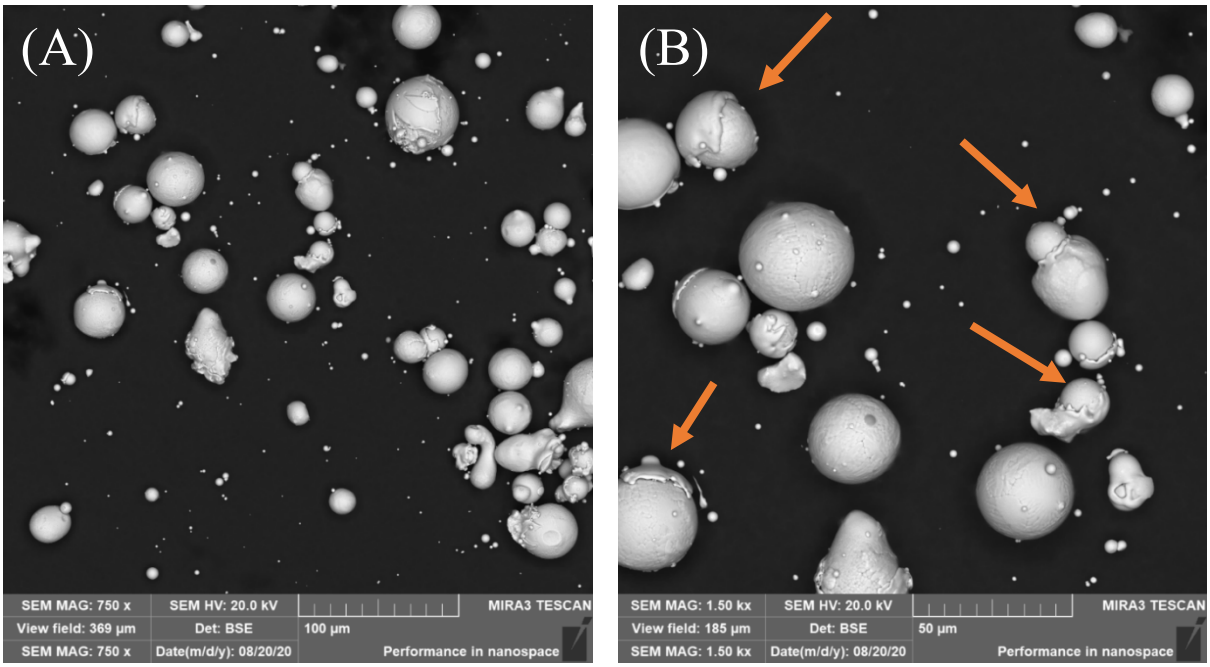

Figure 3: 17-4PH feedstock powder particles as imaged with SEM. (A) 750X magnification, and (B) 1500X magnification. Arrows indicate examples of powder particles that collided during atomization.

All parts used for this research were built on an EOS M280 laser-based powder bed fusion (L-PBF) machine at CIMP-3D. The parts studied included two geometries of interest, namely ASTM Standard E8 [29] subsize rectangular tensile specimen geometry with thicknesses of 2mm ("thin") and 6mm ("standard"). Additional cylindrical parts of 8mm diameter and the same height (100mm) were built and exposed to the same thermal history conditions as the tensile specimens. These cylinders were cut into disks of ~3.75mm thickness post-build for dynamic testing using a Split Hopkinson pressure bar (SHPB) setup.

Two separate builds were created with identical build layouts and sample numbering schemes, aside from the initial build number identifiers. Both builds used standard EOS parameters for 17-4PH stainless steel, including: laser power of 220W, hatch spacing of 0.11mm, scan speed of 755.5mm/s, beam offset of 2µm, and layer thickness of 40µm. In addition to standard building parameters with single full power laser exposures at each build layer, two unique build parameter combinations were explored with the tensile and SHPB sample geometries: double exposure and mixed exposure. Double exposure indicates that the full Z-length of the sample was exposed to secondary laser passes at reduced power for each build layer. Mixed exposure indicates that the bottom half of the Z-length (0-50mm) of each sample was exposed to single full power laser passes, and the top half of the Z-length (50-100mm) of the sample was exposed to additional secondary laser passes at reduced power for each layer. This was performed to create a sharp gradient between as-built thermal histories. A schematic illustrating the differences between standard, double, and mixed exposure is shown in Figure 4.

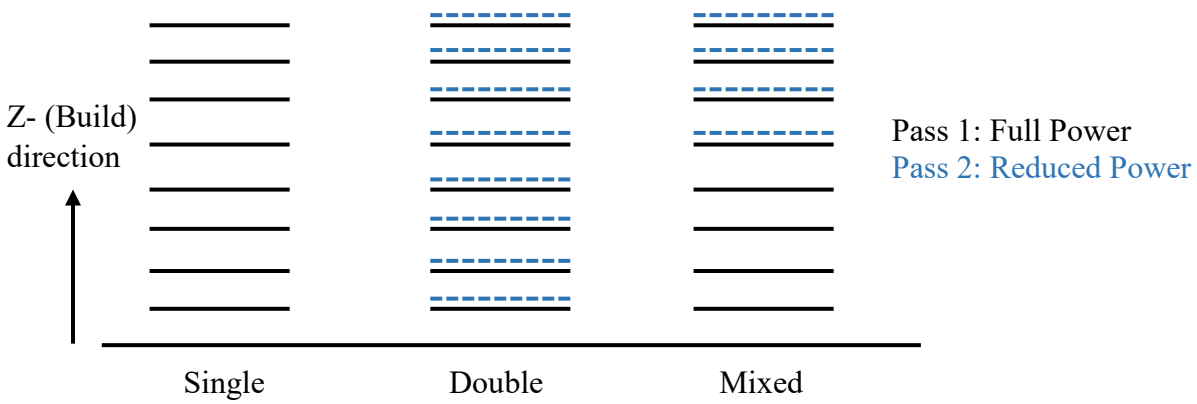

Figure 4: Build parameter combinations for single, double, and mixed exposures.

For build 1, the secondary laser passes were performed at 50% ("half power," 110W) of the standard parameters' laser power. For build 2, the secondary laser passes were performed at 25% ("quarter power," 55W) of the standard parameters' laser power. Each build included three replicates of each tensile thickness (standard and thin) for each build laser exposure combination (single, double, and mixed), and two replicates of the SHPB cylinders at each build laser exposure combination. It should be noted that these parts were built in conjunction with cylindrical lattice geometries used for a different research project. Figure 5 highlights an example build layout. As the key indicates, samples marked in gray were built with single full power laser exposures at each layer, parts marked in green had double laser exposure (half power for build 1, quarter power for build 2), and parts marked in purple experienced mixed laser exposure. A completed build is shown in Figure 6.

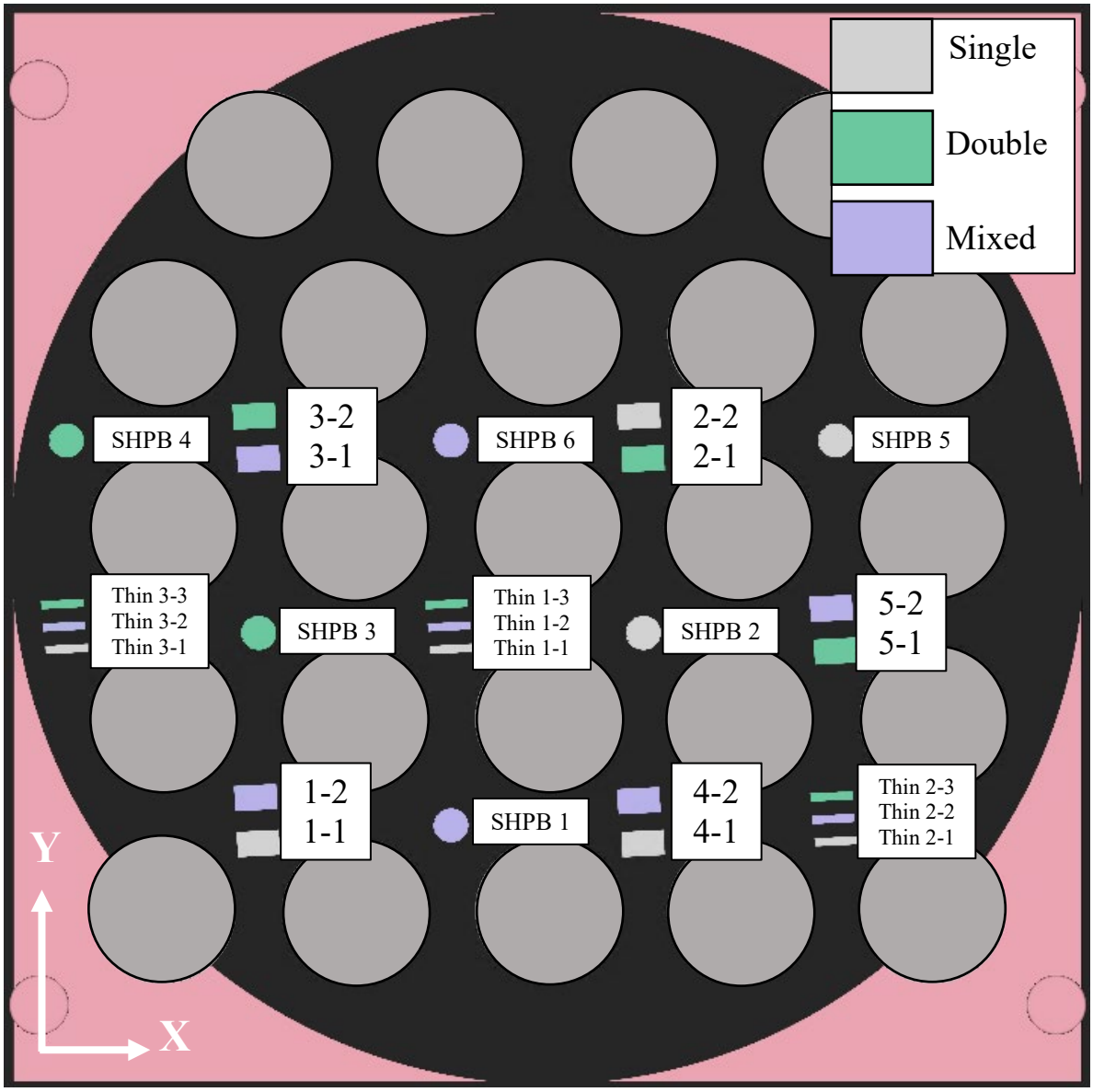

Figure 5: Example build plate layout and naming scheme. Circles indicate cylindrical lattice parts that were used for a separate research study.

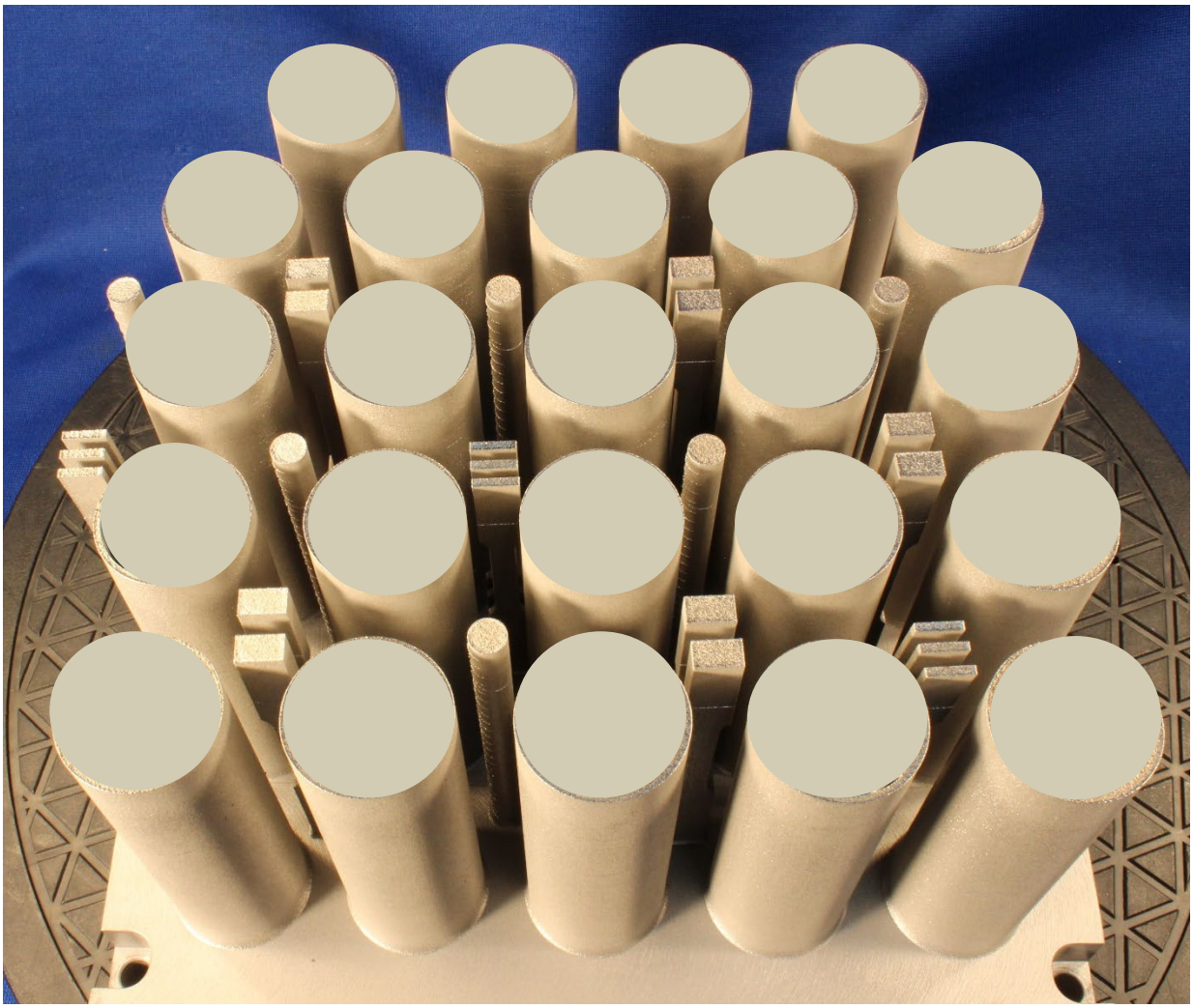

Figure 6: A completed build on the substrate.

Heat Treatment Procedures

The parts used in this study were subjected to the peak aged, highest-strength H900 heat treatment per ASTM Standard A564 [26]. The specifics of the H900 treatment for these builds are:

- Parts all heat treated while remaining attached to the substrate to prevent geometric distortion per ASTM Standard F3301 [34]
- Parts heat treated in a standard air furnace atmosphere per ASM Handbook Volume 4D: *Heat Treating of Irons and Steels* [25]
- Solution anneal
    - Temperature: 1900°F ± 25°F
    - Hold time: 1 hour +15 / -0 minutes
    - Nitrogen cooled to below 90°F
- Age
    - Temperature: 900°F ± 10°F
    - Hold time: 1 hour +15 / -0 minutes
    - Nitrogen cooled to below 90°F

Mechanical Testing Procedures

Mechanical testing was performed to characterize both global and local mechanical response. For global properties, quasi-static uniaxial tensile testing was performed. For local properties, microhardness mapping was used. Additionally, qualitative examination of global mechanical response was completed via fracture surface analysis. Each procedure is expanded upon separately.

Tensile Testing Procedures

All tensile specimens were built and tested according to ASTM Standard E8 [29] using subsize rectangular tensile specimen geometry (flat dogbones) with thicknesses of either 2mm ("thin") or 6mm (standard). The samples were tested on Instron 8801MT servo-hydraulic frame equipped with an Instron 22kip load cell. The tests were conducted in displacement control with a constant X-head rate of 0.05in/min, which translates to a nominal strain rate within the linear elastic region of 0.013in/in/min. An externally mounted Instron 2620-824 axial extensometer with a 40% full-scale strain range was also used. The testing setup is shown in Figure 7.

Figure 7: Quasi-static tensile testing specimen and machine setup.

During all specimen testing, data for tensile force via the load cell, and axial strain via the extensometer was collected at 10Hz. The tensile strain was calculated using input dimensions for the cross-sectional length and width of the gauge region as measured with dial calipers pre-testing. The data was then plotted using Microsoft Excel to determine ultimate tensile strength, elastic modulus, yield strength (via 0.2% linear offset method), and strain at fracture. Statistical analysis of the data across thermal history conditions was performed using Microsoft Excel; more information on the results and statistical analysis are in the *Results, Analysis, and Discussion* section.

Microhardness Mapping Procedures

The microhardness mapping was performed on specimens intended for dynamic compressive testing using the Split Hopkinson pressure bar (SHPB) setup. Due to the similar cross-sectional areas between the tensile specimens (36mm^2 in the gauge length) and the SHPB cylinders (50mm^2), plus the identical heights between them (100mm) it can be assumed that the thermal histories are similar enough for direct comparison.

Four replicates of each thermal history condition (standard, double exposure at half power, and double exposure at quarter power) were each hot mounted together with glass-filled epoxy powder. This resulted in three plastic pucks, each containing four individual samples, for a total of 12 microstructural characterization samples. The SHPB disks were mounted across the XZ/YZ plane such that the surface being examined included a cross-sectional view across the build direction layers. The samples were mechanically polished to a surface finish of 1µm with an automated polishing machine using standard metallographic procedures per ASTM Standard E3 [35]. A schematic of the sample mount used for this testing is shown in Figure 8.

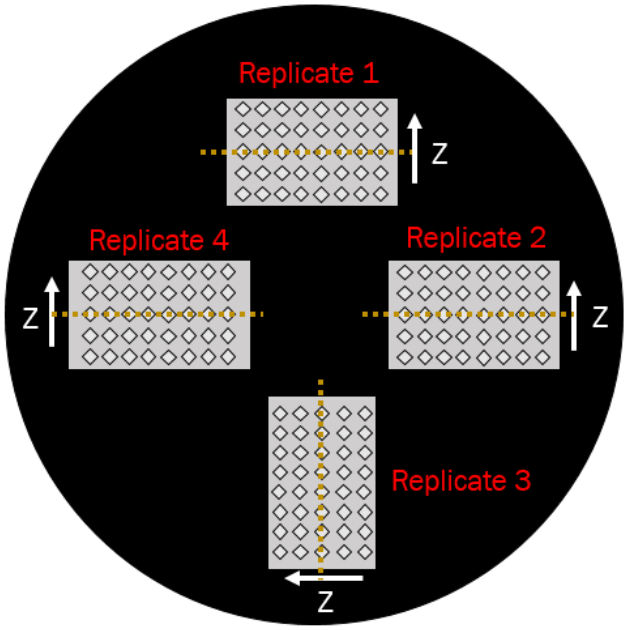

Figure 8: Representative sample mount with four replicates of a given thermal history. The diamonds represent the microhardness indentation map pattern, the gold dotted lines indicate where along the build height the exposure strategy was changed for mixed specimens, and the white arrows indicate the build (Z-) direction.

All microhardness measurements were performed according to ASTM Standard E92 for Vickers hardness [36]. Using a Wilson VH3100 Vickers automated hardness tester, ~550-600 indents in a rectangular grid were performed per sample with a 500g load, 10s dwell time, and 0.1778mm (0.007in) spacing. The testing setup is shown in Figure 9. The resulting microhardness maps are in the *Results, Analysis, and Discussion* section.

Figure 9: Microhardness mapping setup.

Fracture Surface Analysis

The fracture surfaces of the tensile specimens were examined with a TESCAN MIRA high-resolution analytical SEM using a secondary electron detector. A 10.0kV accelerating voltage under high vacuum was used, and micrographs were taken at various magnifications until 5000X (a view field of 55.4μm) was established as an appropriate representation of the fracture behavior. Representative fracture surface micrographs are documented in the *Results, Analysis, and Discussion* section.

Microstructural Characterization

Microstructural characterization was performed both qualitatively and quantitatively. All microstructural analysis was performed on the specimens intended for dynamic compressive testing using the Split Hopkinson pressure bar (SHPB) setup as described in the *Microhardness Mapping Procedures* section. For qualitative analysis, both optical and electron microscopy was

performed on etched samples. For quantitative analysis, electron backscatter diffraction (EBSD) measurements were used. Each procedure is expanded upon separately.

Qualitative Metallography

The same samples and sample preparation techniques as described in the *Microhardness Mapping Procedures* section were used for qualitative metallographic analysis. Upon completion of polishing to a surface finish of 1µm, the samples were immersion etched with Kalling's Reagent for 15-20s. Representative micrographs at 800X were taken both optically with a Keyence VHX-6000 microscope and via secondary electron imaging with a TESCAN MIRA high-resolution analytical SEM at 10.0kV accelerating voltage. Representative micrographs are documented in the *Results, Analysis, and Discussion* section.

Quantitative Metallography

The same samples and sample preparation techniques as described in the *Microhardness Mapping Procedures* section were used for qualitative metallographic analysis. Upon completion of polishing to a surface finish of 1µm, an overnight vibratory final polish to a surface finish of 0.02µm was performed prior to electron backscatter diffraction (EBSD) measurements.

EBSD measurements were performed on a ThermoScientific Apreo S field emission scanning electron microscope (FESEM). The following settings were used for EBSD measurements:

- Specimen tilt: 70°
- Magnification: 2000X (≈ 135µm by 200µm scanning area)
- Beam current: 3.2nA
- Accelerating voltage: 20.0kV
- Step size: 0.5µm
- Possible phases: body-centered cubic (bcc) iron and face-centered cubic (fcc) iron
- Grain boundary threshold: 10° misalignment

Post processing of data was completed with Oxford Instruments' AZtec software, Microsoft Excel, and MATLAB. Data of interest from AZtec included grain area minimum, maximum, mean, and standard deviation, as well as ASTM grain size and grain equivalent circle diameter. Excel was used to add 95% confidence intervals on the mean grain size and grain equivalent circle diameter. MATLAB was used for data visualization and the full quantitative statistical analysis using logarithmic grain size distributions. More information on the results and statistical analysis are in the *Results, Analysis, and Discussion* section.

Results, Analysis, and Discussion

The related results for each type of mechanical testing or microstructural analysis will be expanded upon as subsections in this section for clarity.

Tensile Testing Results

Four global mechanical properties were analyzed to determine the effectiveness of heat treatment normalizing different L-BPF thermal histories: 0.2% offset yield strength (YS), elastic modulus, ultimate tensile strength (UTS), and strain at break. Figure 10 shows a summary of each of these tensile properties measured through quasi-static uniaxial tensile testing. The color of each data point indicates which laser scan strategy was used to produce that specimen. The shape of the data point indicates from which build each specimen was produced. Visually, there appears to be

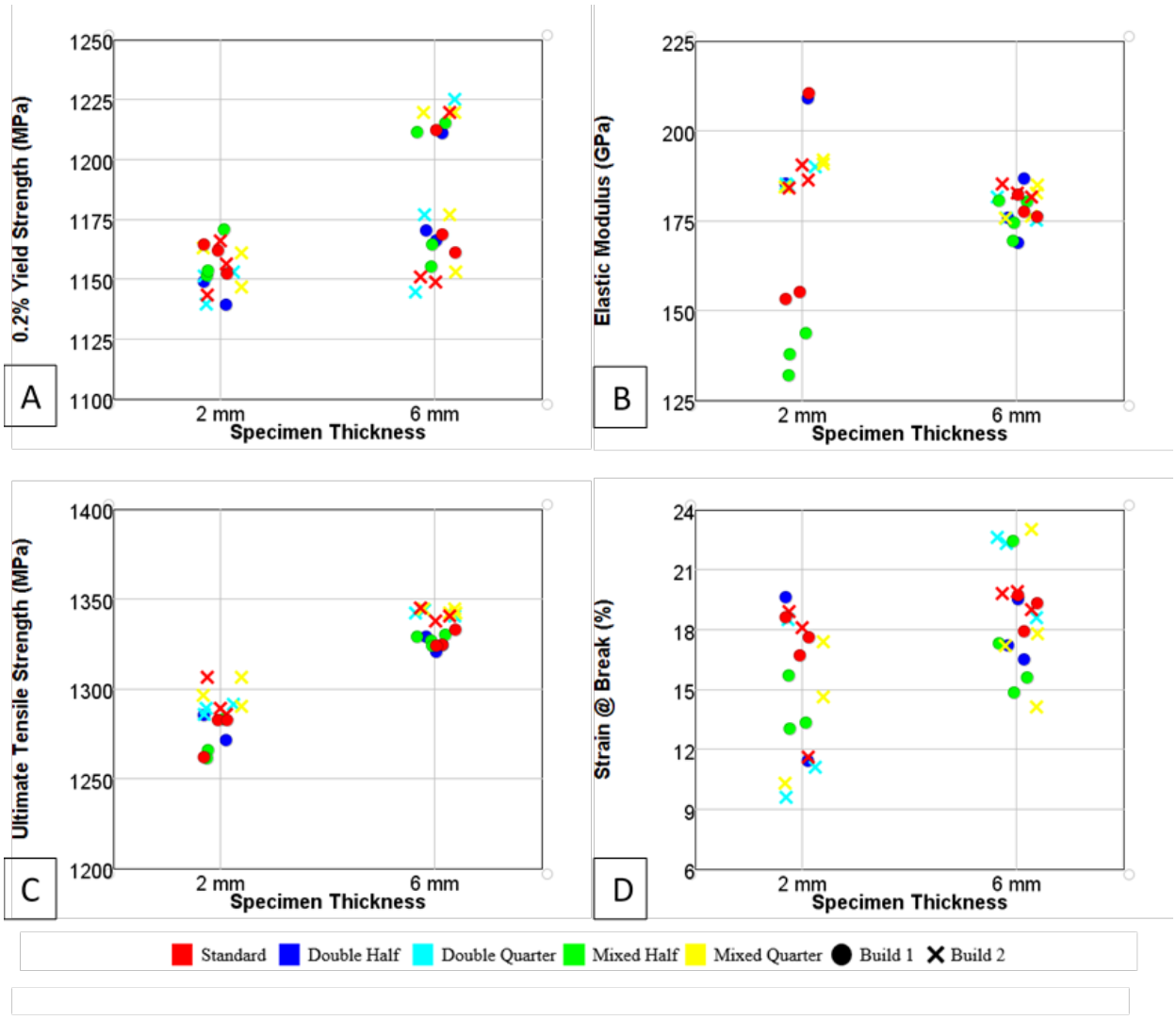

Figure 10: Scatter plots of tensile testing results. (A) shows 0.2% yield strength, (B) shows elastic modulus, (C) shows UTS, (D) shows strain at break. Changes in build parameters are indicted with different colors. Shape of the data point indicates build number.

no significant difference in mechanical response between the different scan strategies, which would indicate that H900 is an effective heat treatment for L-PBF produced 17-4PH parts.

To confirm this observation, statistical analysis for the mechanical testing data was completed using Microsoft Excel. Thermal history and thickness combination categories included: standard 6mm, double half 6mm, double quarter 6mm, mixed half 6mm, mixed quarter 6mm, standard 2mm, double half 2mm, double quarter 2mm, mixed half 2mm, and mixed quarter 6mm. Mechanical testing metrics of interest included the 0.2% offset yield strength, elastic modulus, ultimate tensile strength, and elongation at break. The sample size in most categories prohibited a normality test, so normality was assumed for this analysis. Next, an F-test was completed for each category compared to standard to verify equivalence of variances. Finally, a paired two-tail t-test was performed compared to standard to assess the equivalence of the means of each sample category. The results for each of these tests is seen in Table 3 for the 6mm thick samples and Table 4 for the 2mm thick samples. 95% confidence intervals reported on mechanical property means in Tables 3 and 4 were calculated using the t-distribution.

Table 3: Mechanical testing statistical analysis results for the 6mm thick samples.

	0.2% Yield Strength			Elastic Modulus			Ultimate Tensile Strength			Strain @ Break		
	Mean (MPa)	F-test	p-value	Mean (GPa)	F-test	p-value	Mean (MPa)	F-test	p-value	Mean (%)	F-test	p-value
Standard 6mm	1176.8 ± 5.39			180.8 ± 0.60			1334.0 ± 1.49			19.3 ± 0.13		
Double Half 6mm	1182.2 ± 7.75	0.86	0.80	176.9 ± 2.82	0.08	0.36	1324.5 ± 1.29	0.39	0.12	17.7 ± 0.49	0.16	0.08
Double Quarter 6mm	1182.2 ± 12.7	0.55	0.83	177.4 ± 1.13	0.82	0.22	1342.2 ± 0.54	0.08	0.16	21.2 ± 0.70	0.05	0.09
Mixed Half 6mm	1186.4 ± 7.41	0.93	0.65	176.0 ± 1.27	0.38	0.12	1327.2 ± 0.64	0.08	0.17	17.5 ± 0.81	0.01	0.25
Mixed Quarter 6mm	1192.3 ± 7.89	0.84	0.48	179.9 ± 1.09	0.56	0.73	1343.4 ± 0.28	0.01	0.07	18.0 ± 0.88	0.01	0.43

Table 4: Mechanical testing statistical analysis results for the 2mm thick samples.

	0.2% Yield Strength			Elastic Modulus			Ultimate Tensile Strength			Strain @ Break		
	Mean (MPa)	F-test	p-value	Mean (GPa)	F-test	p-value	Mean (MPa)	F-test	p-value	Mean (%)	F-test	p-value
Standard 2mm	1157.3 ± 1.49			179.9 ± 3.79			1284.7 ± 2.49			16.9 ± 0.47		
Double Half 2mm	1143.8 ± 3.52	0.96	0.10	197.0 ± 8.71	0.96	0.36	1278.3 ± 5.03	0.94	0.59	15.5 ± 2.99	0.17	0.63
Double Quarter 2mm	1148.0 ± 2.25	0.91	0.16	186.5 ± 0.91	0.03	0.63	1288.9 ± 0.87	0.07	0.65	13.1 ± 1.49	0.27	0.16
Mixed Half 2mm	1158.5 ± 3.32	0.62	0.85	137.7 ± 1.82	0.13	0.02	1270.0 ± 3.63	0.88	0.17	14.0 ± 0.46	0.49	0.13
Mixed Quarter 6mm	1156.9 ± 2.82	0.81	0.96	189.0 ± 1.29	0.07	0.51	1343.4 ± 0.28	0.54	0.20	14.1 ± 1.12	0.54	0.22

This analysis indicated that there were no significant differences in tensile strength values across thermal history conditions after H900 heat treatment. T-tests comparing each scan strategy with standard parameters for either the 6mm or 2mm thick specimen report p-values above 0.05, indicating a 95% confidence that post heat treatment, all of the specimen come from populations with identical means. There is one exception, elastic modulus of the 2mm mixed half power specimens. Because the other mechanical properties for this same set of specimens do not report a statistically significant difference, and the small sample size, this one result is considered to be an outlier.

It is also important to note the fracture location for each of the tensile specimens to identify any potential localized differences in mechanical response. For example, the largest difference in thermal history of any samples should occur in the mixed exposure specimens at the build's halfway transition in Z-length (50mm) where the exposure settings changed from standard single exposure to a double exposure with either half or quarter laser power. It follows that if the as-built thermal history remained after heat treatment, the samples should have all broken near the middle of the gauge length where that transition occurred. Figure 11 and Figure 12 below show that none of the mixed exposure samples, with either half power (Figure 11) or quarter power (Figure 12) secondary exposures, failed at the center of the gauge length for either specimen thickness.

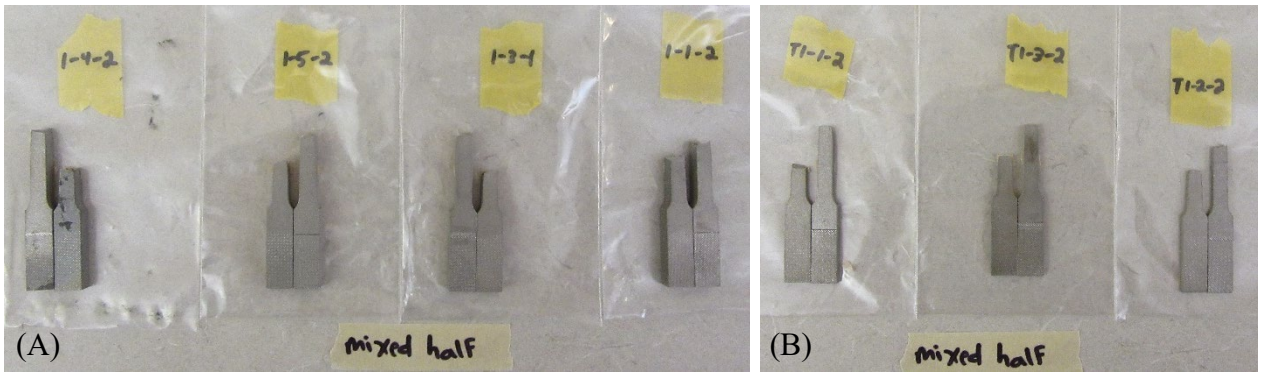

Figure 11: Fractured tensile specimens with mixed exposure, where the bottom half of the sample received standard single laser exposure and the top half of the sample received half laser power secondary exposure. (A) 6mm standard width specimens, and (B) 2mm thin width specimens.

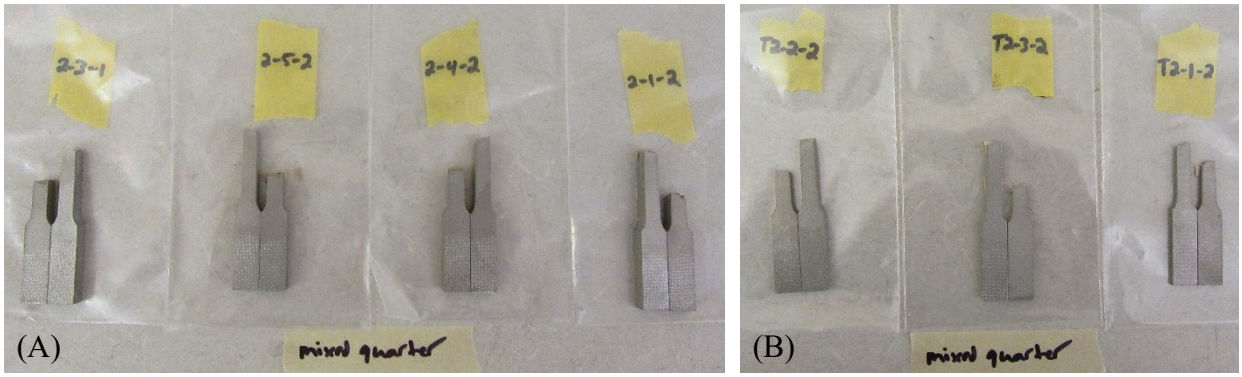

Figure 12: Fractured tensile specimens with mixed exposure, where the bottom half of the sample received standard single laser exposure and the top half of the sample received quarter laser power secondary exposure. (A) 6mm standard width specimens, and (B) 2mm thin width specimens.

However, upon further inspection, there does appear to be a pattern in the location of where the mixed exposure samples fractured. When the samples are laid out such that all of the halves that were attached to the substrate are on the same side, every mixed exposure specimen fractured in the region of the gauge length corresponding to the standard parameter settings. This is shown in Figure 13. It should be noted that for tensile testing, the half of the tensile specimen that was attached to the substrate was randomized for whether it was placed in the stationary or moving machine grip.

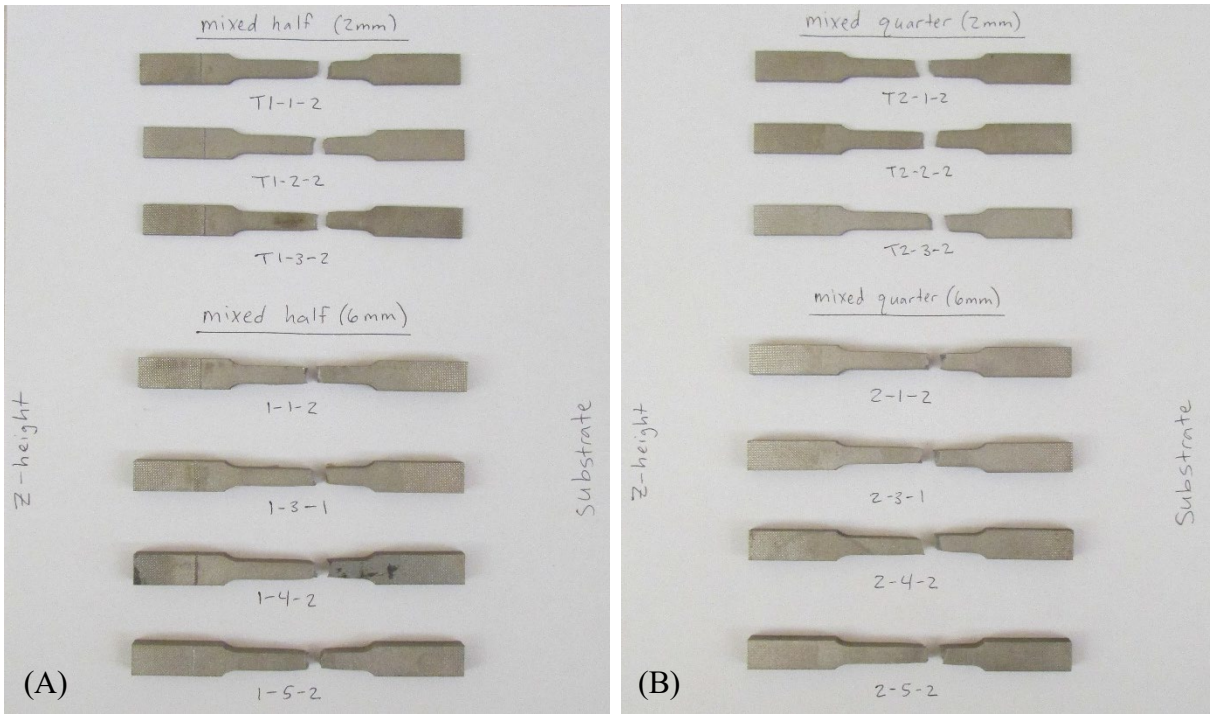

Figure 13: Mixed exposure samples aligned by halves closest to the substrate. (A) Mixed half power specimens, and (B) mixed quarter power specimens.

For comparison, all double and standard exposure samples fractured in a more randomized fashion, and no obvious patterns or correlations to build direction were found. This is illustrated by the samples shown in Figure 14 and Figure 15 for double exposure and standard exposure, respectively. It is possible that the change in exposure patterns halfway through the part changed the local mechanical properties, but the global properties remained the same due to breaking in the weaker half of the sample. Additionally, the properties of the specimen with multiple laser exposures throughout the specimen did not exhibit different mechanical properties than the specimens with a mixed exposure scan pattern. More investigation of local properties and microstructural differences in the tensile specimens is needed to confirm if there is a local change in mechanical properties at the scan pattern change boundary. If this is the case, it is unclear why the double exposure samples did not show a change in global mechanical properties due to the difference in exposure across the entire length of the sample compared to the standard exposure samples. More experimentation would be required to verify this.

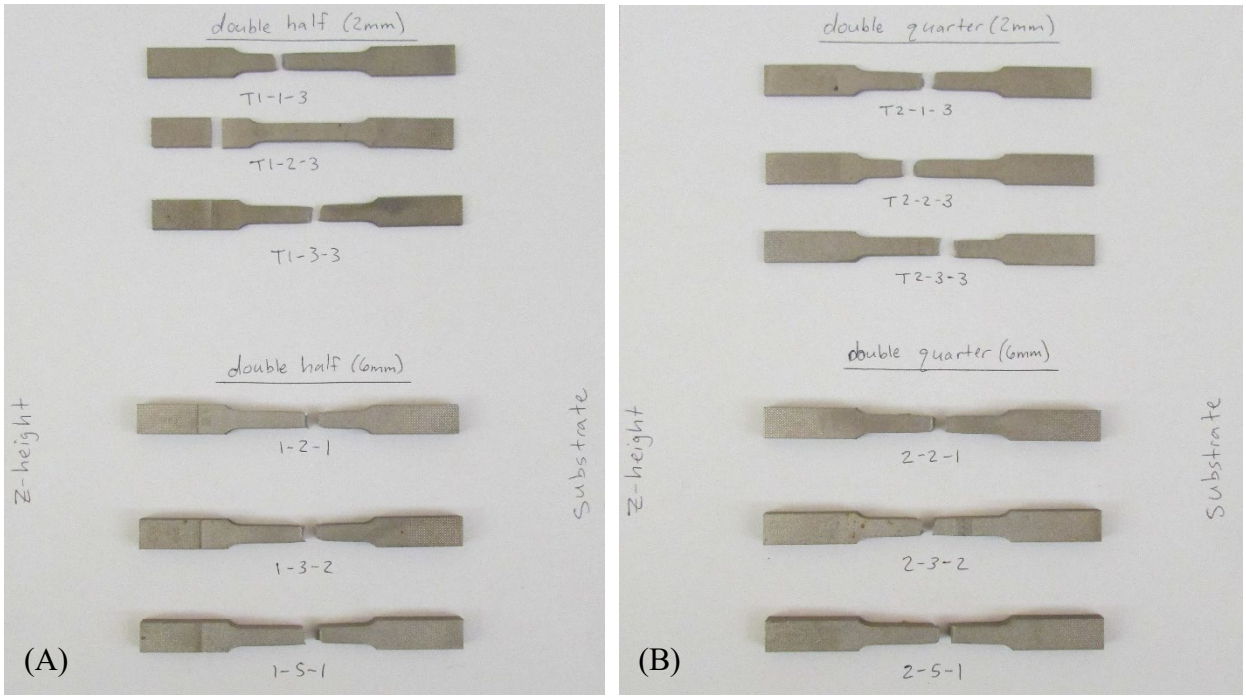

Figure 14: Double exposure samples aligned by halves closest to the substrate. (A) Double half power specimens, and (B) double quarter power specimens.

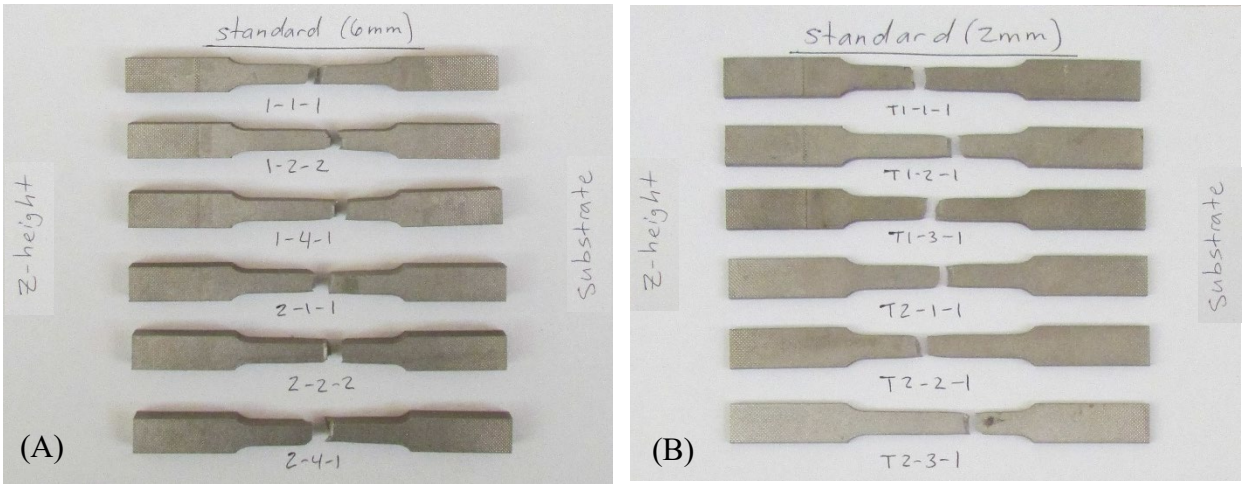

Figure 15: Standard exposure samples aligned by halves closest to the substrate. (A) Standard 6mm specimens, and (B) standard 2mm specimens.

Microhardness Mapping Results

Local mechanical response was explored using the SHPB samples. Four replicates of each scan strategy were examined with microhardness mapping. The resulting maps are shown in Figure 16 for single exposure (A), alternating half exposure (B), and alternating quarter exposure (C) scan strategies.

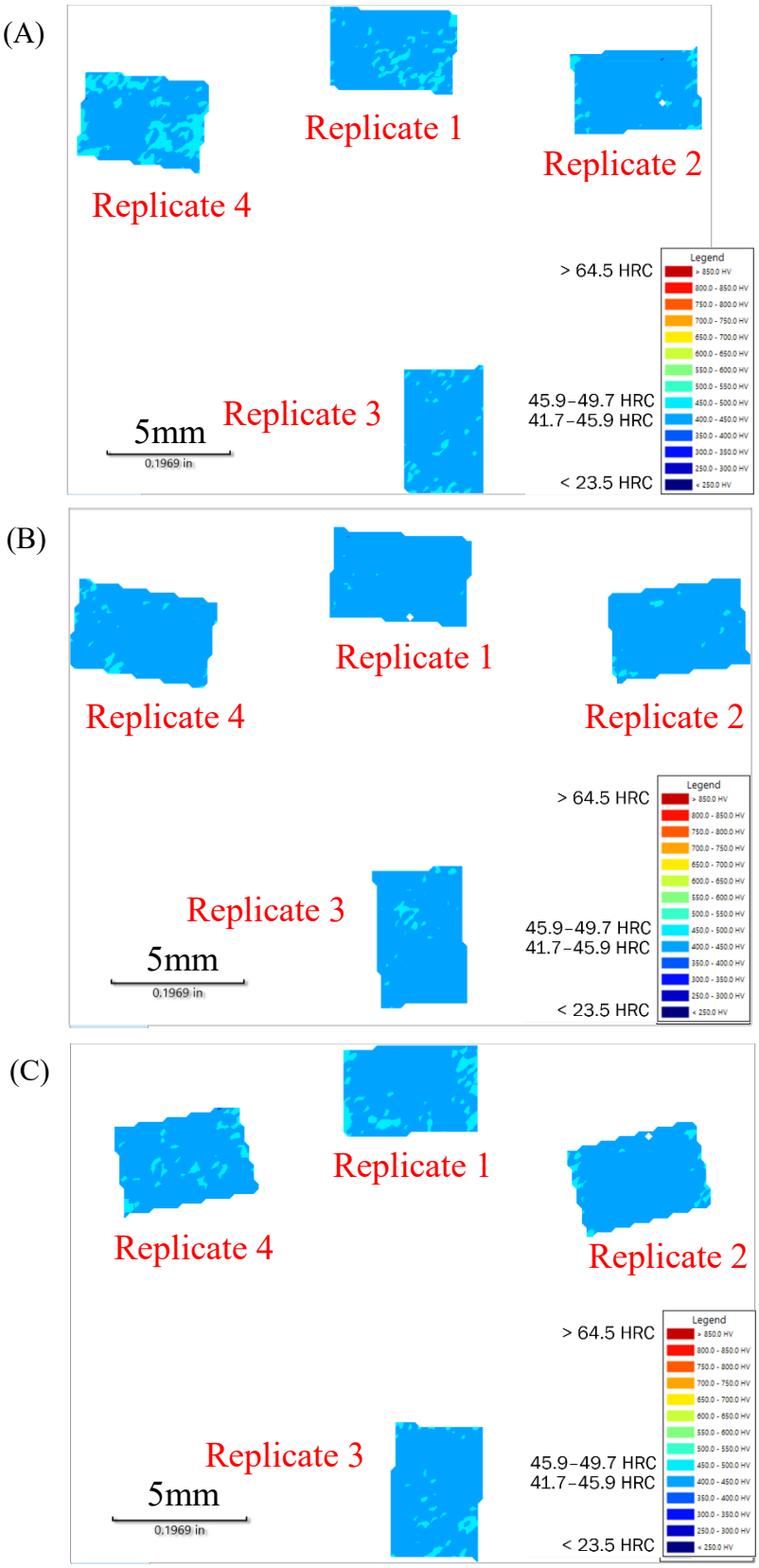

Figure 16: Microhardness mapping results for (A) single exposure, (B) alternating half exposure, and (C) alternating quarter exposure.

The color scale in Vickers hardness (HV) was selected as the full range of Rockwell C hardness (HRC) values to highlight the homogeneity across the samples, rather than modifying the scale to show larger differences in local microhardness that may sway the interpretation of the results to indicate that there were significant differences in local properties across the scan strategies. Each of the replicates from the scan strategies shows a local microhardness equivalent to ~41.7-49.7 HRC, which is consistent with the expected average hardness after peak aging of ~45 HRC. Some inhomogeneity is expected with L-PBF due to pores and other defects inherent to the process.

Fracture Surface Examination Results

A 10.0kV accelerating voltage under high vacuum was used to examine all of the tensile specimens' fracture surfaces Micrographs were taken using secondary electrons at 5000X (a view field of 55.4μm). Each of the scan strategies in both thin and standard geometries exhibited fracture surfaces typical of ductile failure. Representative tensile testing fracture surfaces for standard full power exposure (A), double exposure at half power (B), and double exposure at quarter power (C) are shown in Figure 17.

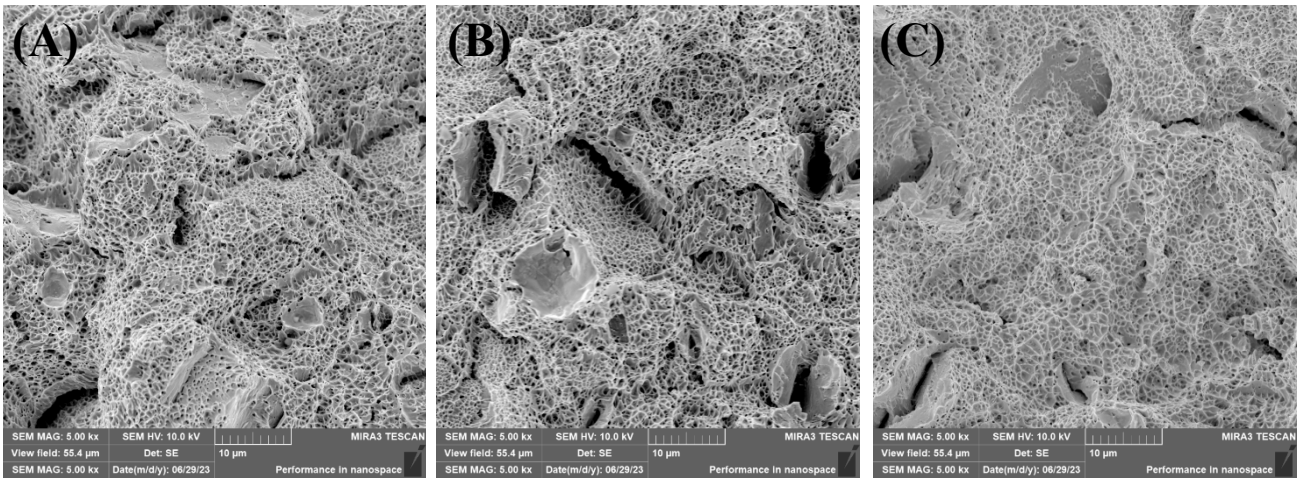

Figure 17: Representative tensile testing fracture surfaces for specimens built with (A) standard full power exposure, (B) double exposure at half power, and (C) double exposure at quarter power.

Qualitative Microstructural Characterization Results

Representative optical (A) and SEM (B) micrographs of standard single full power exposure samples etched with Kalling's Reagent at 800X are shown in Figure 18.

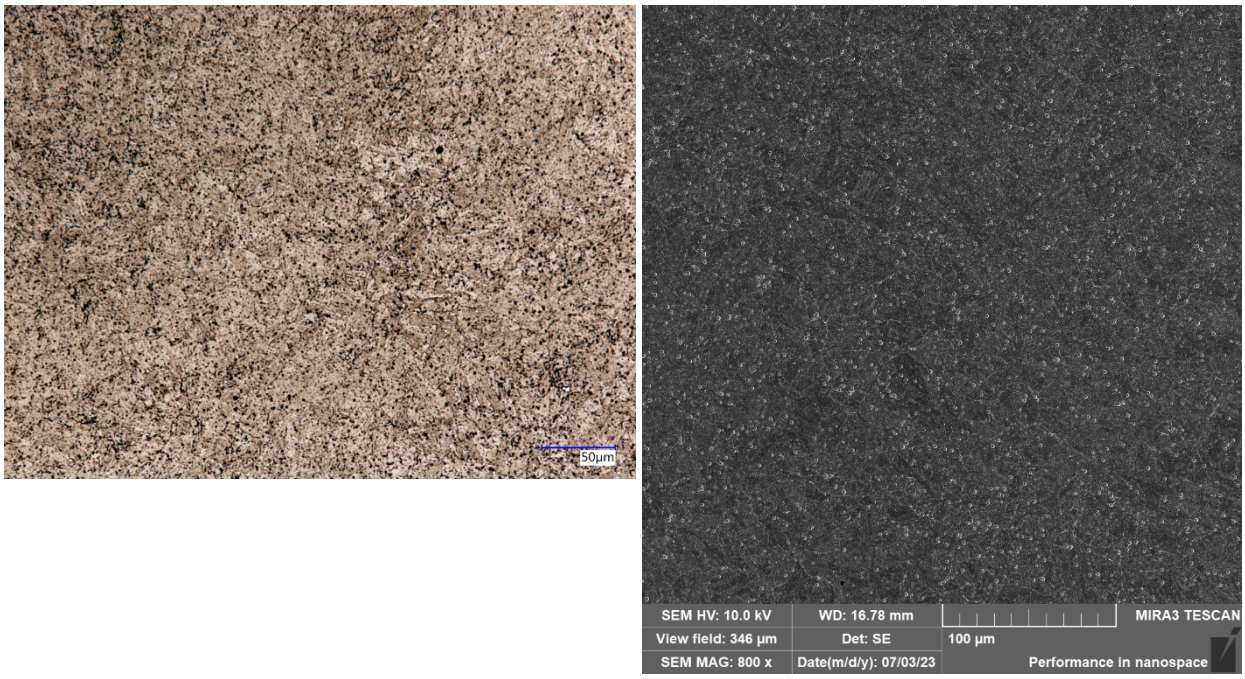

Figure 18: Representative optical (A) and SEM (B) micrographs of standard single full power exposure samples etched with Kalling's Reagent at 800X.

The micrographs illustrate the presence of a fully martensitic matrix with the presence of large, dispersed carbides throughout. Energy dispersive x-ray spectroscopy (EDS) mapping was not performed to assess the allying element forming the carbides, but it is anticipated to be niobium. Additionally, imaging at a high enough magnification to see the copper carbides was not possible with the optical technique and was therefore also skipped for the SEM. The EDS mapping for carbides and copper precipitates should be explored in future work.

Qualitative Microstructural Characterization Results

While collecting EBSD data, several maps are available to visualize the data. For this particular study, the Z-direction inverse pole figures (IPF) coloring overlaid with grain boundaries provide the best visual representation of the microstructural features that were being measured, including grain size, grain morphology, phase identification, and grain orientation. All samples measured (four replicates of each thermal history condition) resulted in phase identifications of 100% body-centered cubic (bcc) iron, indicating that no retained austenite was present and the sample microstructural matrices were completely aged martensite. The grain size measurements from AZtec reported by area are shown in Table 5. Similarly, the grain morphology measurements from AZtec reported by equivalent circle diameter are listed in Table 6. Note that the grains that intersected the border of the image area were not counted for either measurement. Both tables include an "average" row that considers the results of all four replicates in each thermal history category.

Table 5: Grain measurement by area in μm^2 as reported by AZtec.

Grain Measurement by Area							
Category	**Replicate**	**Grain Count**	**Mean Area (μm^2)**	**Min Area (μm^2)**	**Max Area (μm^2)**	**Std. Dev. (μm^2)**	**ASTM 2627 Grain Size**
Standard	1	1049	20.3	2.5	483.3	37.4	12.6
	2	1073	20.6	2.5	751.3	41.8	12.6
	3	1154	17.5	2.5	380.5	29.2	12.8
	4	1090	19.6	2.5	554.8	42.4	12.6
	"Average"	*1091.5*	*19.5*	*2.5*	*542.5*	*37.7*	*12.7*
Mixed Half	1	907	22.4	2.5	425.5	42.1	12.5
	2	1028	19.6	2.5	506.5	39.9	12.6
	3	972	20.9	2.5	557.5	40.9	12.6
	4	947	22.0	2.5	694.8	49.1	12.5
	"Average"	*963.5*	*21.2*	*2.5*	*546.1*	*43.0*	*12.6*
Mixed Quarter	1	989	19.7	2.5	337.3	33.8	12.6
	2	936	22.4	2.5	474.0	42.5	12.5
	3	1224	16.8	2.5	329.5	29.4	12.9
	4	943	20.3	2.5	729.3	44.5	12.6
	"Average"	*1023.0*	*19.8*	*2.5*	*467.5*	*37.6*	*12.7*

Table 6: Grain measurement by equivalent circle diameter in µm as reported by AZtec.

Grain Measurement by Equivalent Circle Diameter						
Category	**Replicate**	**Grain Count**	**Min Circle Diameter (µm)**	**Max Circle Diameter (µm)**	**Std. Dev. (µm)**	**Mean Circle Diameter (µm)**
Standard	1	1049	1.8	24.8	2.8	4.2
	2	1073	1.8	30.9	3.0	4.2
	3	1154	1.8	22.0	2.6	4.0
	4	1090	1.8	26.6	2.9	4.1
	"Average"	*1091.5*	*1.8*	*26.1*	*2.8*	*4.1*
Mixed Half	1	907	1.8	23.3	3.1	4.3
	2	1028	1.8	25.4	2.9	4.1
	3	972	1.8	26.6	3.0	4.2
	4	947	1.8	29.7	3.2	4.2
	"Average"	*963.5*	*1.8*	*26.3*	*3.1*	*4.2*
Mixed Quarter	1	989	1.8	20.7	2.8	4.2
	2	936	1.8	24.6	3.1	4.4
	3	1224	1.8	20.5	2.5	3.9
	4	943	1.8	30.5	3.0	4.1
	"Average"	*1023.0*	*1.8*	*24.1*	*2.9*	*4.2*

Finally, Table 7 combines the data from all four replicates of each thermal history category to get a true average and associated 95% confidence interval for both the area and equivalent circle diameters of the grain size measurements.

Table 7: Grain measurement by area (μm^2) and equivalent circle diameter (μm) as reported by Aztec for each thermal history category combined by associated replicates.

Grain Area							
Category	**Grain Count**	**Min Area (μm^2)**	**Max Area (μm^2)**	**Std. Dev. (μm^2)**	**95% Confidence Lower Limit Mean Area (μm^2)**	**Mean Area (μm^2)**	**95% Confidence Upper Limit Mean Area (μm^2)**
Standard	4366	2.5	751.3	37.9	18.4	19.5	20.6
Mixed Half	3854	2.5	694.8	43.1	19.8	21.2	22.5
Mixed Quarter	4092	2.5	729.3	37.5	18.4	19.6	20.7

Grain Equivalent Circle Diameter							
Category	**Grain Count**	**Min Circle Diameter (μm)**	**Max Circle Diameter (μm)**	**Std. Dev. (μm)**	**95% Confidence Lower Limit Mean Circle Diameter (μm)**	**Mean Circle Diameter (μm)**	**95% Confidence Upper Limit Mean Circle Diameter (μm)**
Standard	4366	1.8	30.9	2.8	4.0	4.1	4.2
Mixed Half	3854	1.8	29.7	3.1	4.1	4.2	4.3
Mixed Quarter	4092	1.8	30.5	2.8	4.0	4.1	4.2

The IPF-colored grain maps for the standard, mixed half power, and mixed quarter power samples are shown in Figure 19, Figure 20, and Figure 21 respectively. The build direction is indicated by the white arrow; note that since all four replicates for each thermal history condition were hot mounted together in a single 1.5" diameter specimen, it was not always possible to have +Z in the same direction and still have the required distance from the sample to the detector. Each micrograph has approximate dimensions of 135µm by 200µm. The black pixels correspond to no identified solutions for the proposed phases (bcc iron and fcc iron) in any orientation. The solution rate was 90% or higher for all measured samples.

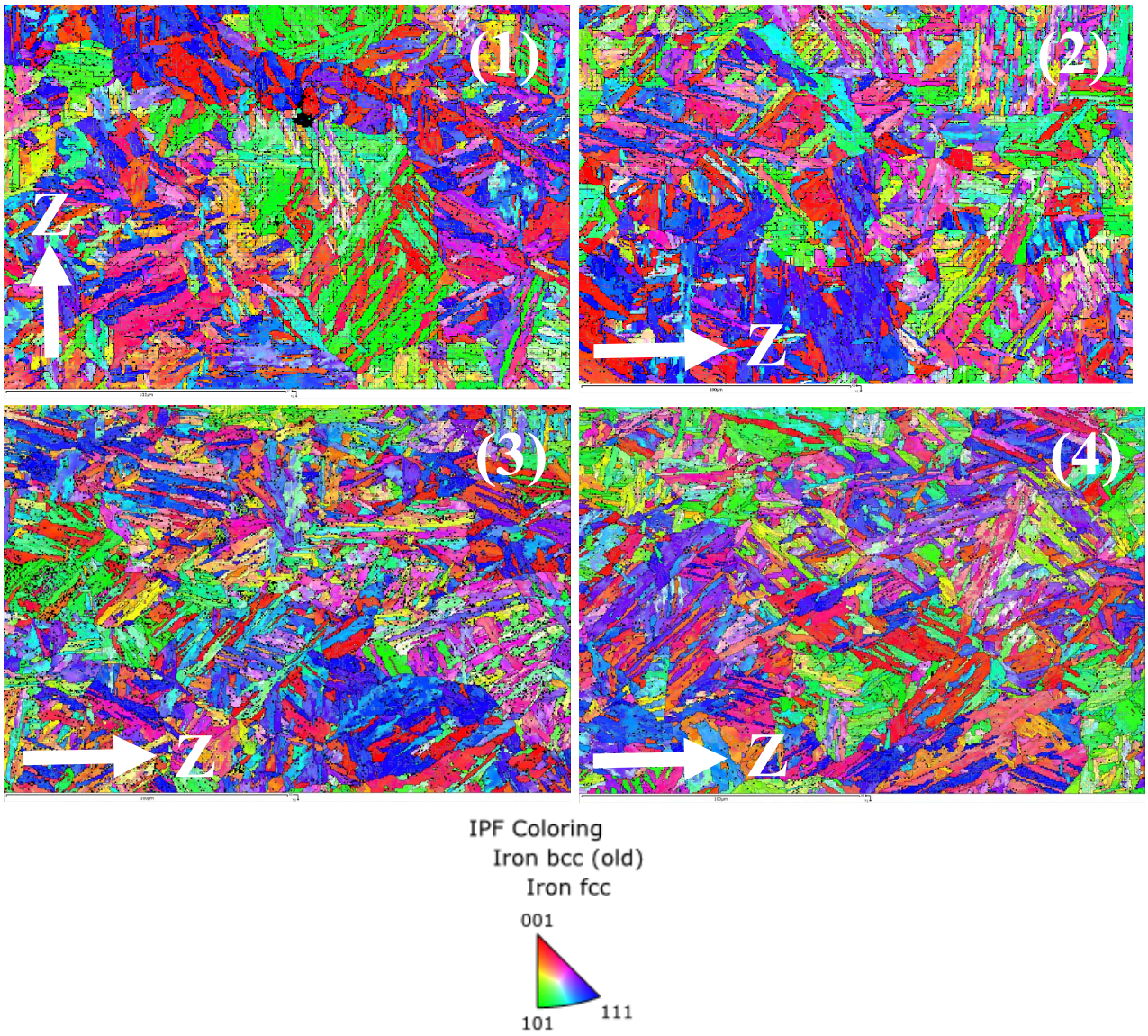

Figure 19: Z-direction inverse pole figure colored maps overlaid with grain boundaries for standard exposure specimens. The numbers in the upper right-hand corners correspond to the replicate number.

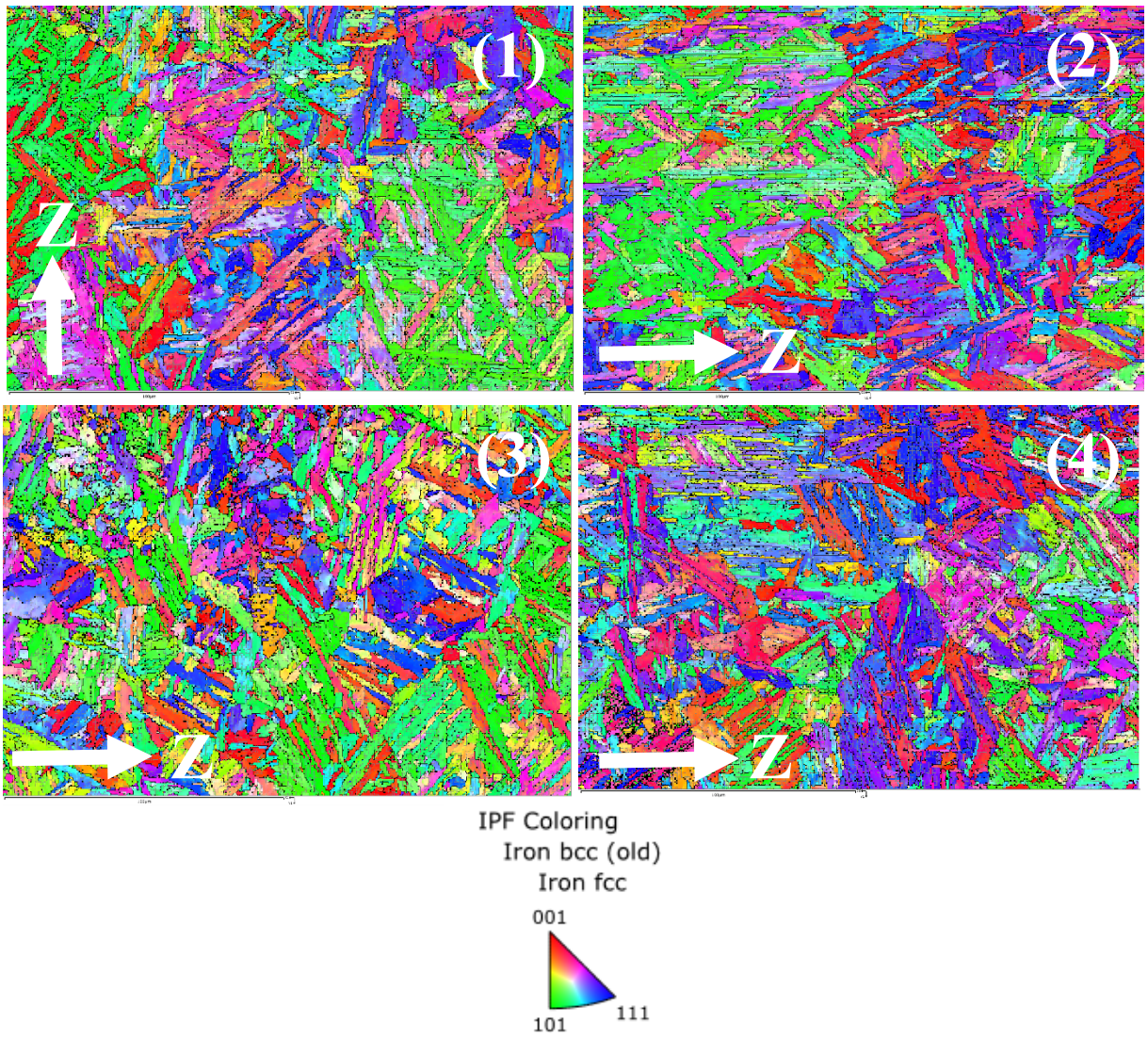

Figure 20: Z-direction inverse pole figure colored maps overlaid with grain boundaries for mixed half exposure specimens. The numbers in the upper right-hand corners correspond to the replicate number.

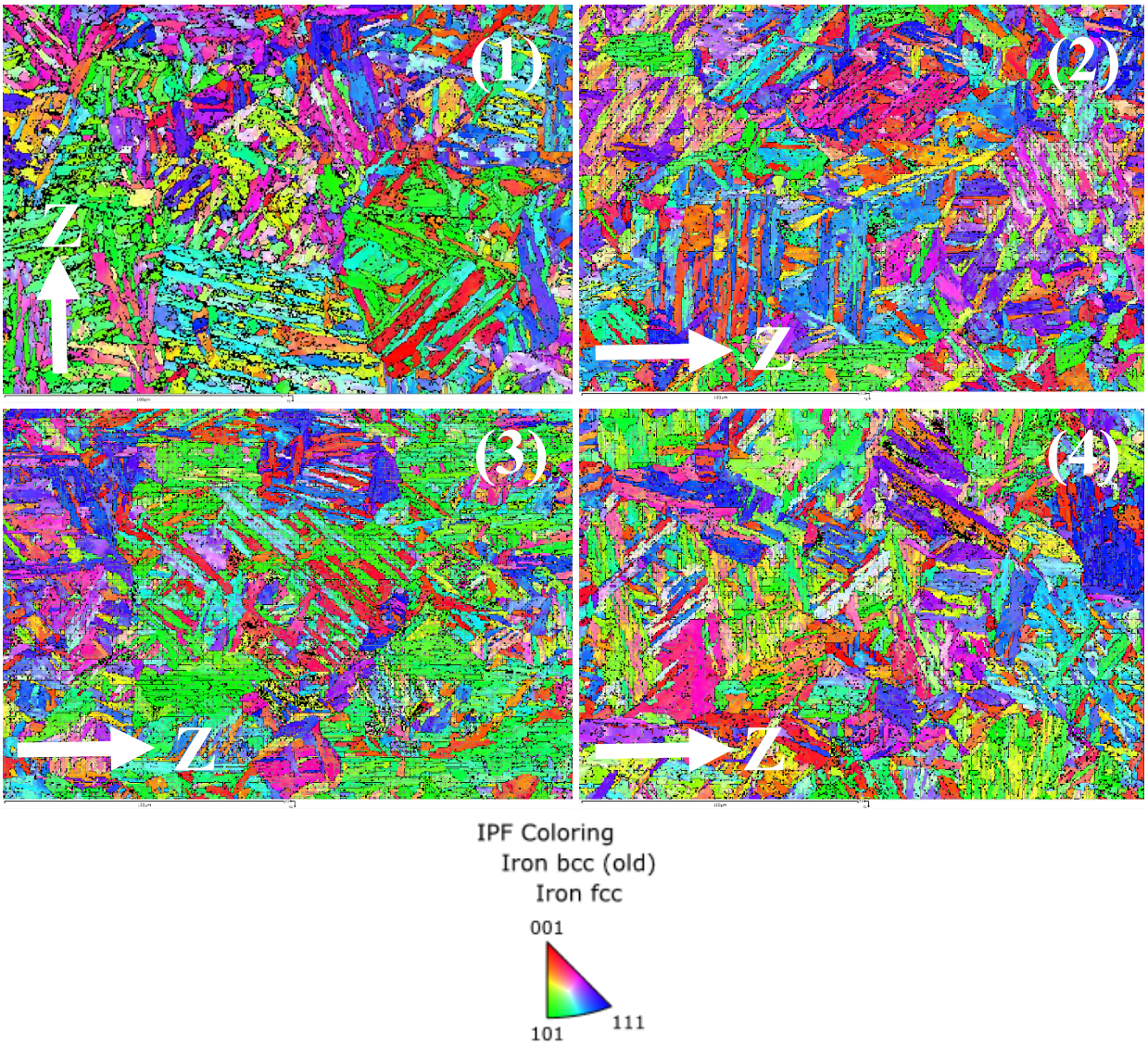

Figure 21: Z-direction inverse pole figure colored maps overlaid with grain boundaries for mixed quarter exposure specimens. The numbers in the upper right-hand corners correspond to the replicate number.

Microstructural Characterization Analysis and Discussion

The statistical analysis for the microstructural characterization data was completed using MATLAB. Thermal history categories included: standard exposure ("single power"), mixed alternating standard and half power exposure ("half power"), and mixed alternating standard and quarter power exposure ("quarter power"). The microstructural features of interest included phase identification, grain size by area, and grain morphology by equivalent circle diameter. Since all phases measured were bcc, no statistical analysis was necessary to confirm that the phases were equivalent across all samples, so only grain area and equivalent circle diameters were analyzed further. Due to the nature of grain size measurements, a logarithmic distribution was used instead of a normal distribution for this data analysis.

First, to better visualize the data distribution, normalized histograms for each of the three categories, including all four replicates, were created for both the grain areas and grain equivalent circle diameters. These can be seen in Figure 22 and Figure 23, respectively.

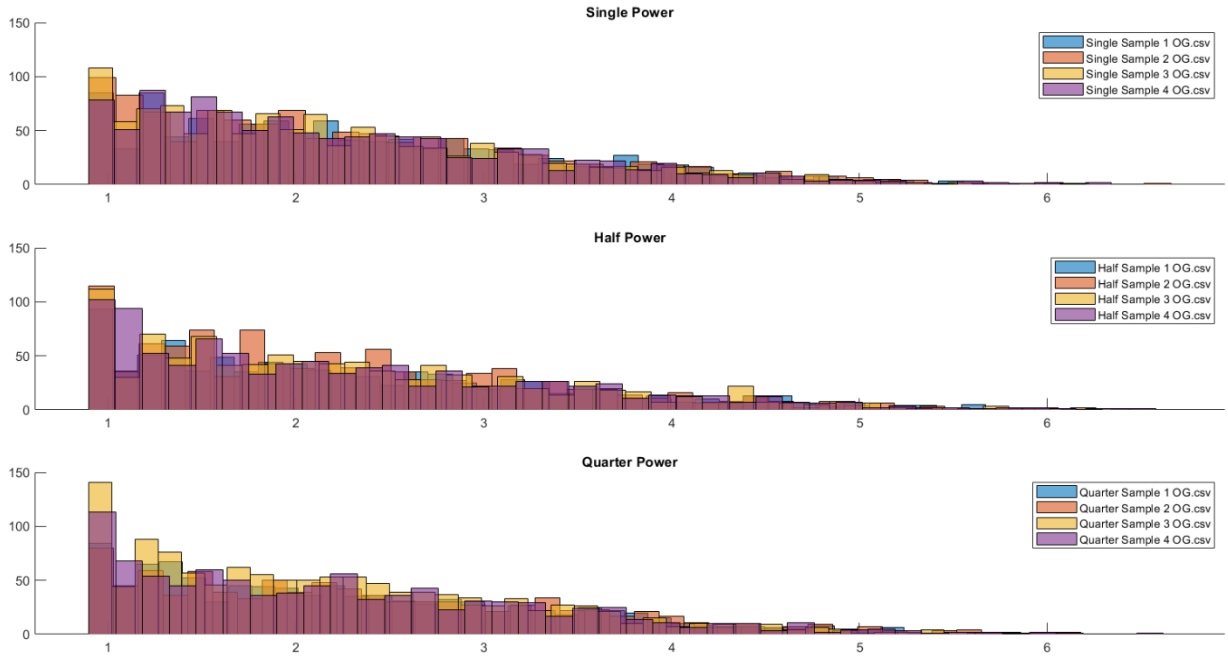

Figure 22: Log grain area normalized histograms by thermal history category.

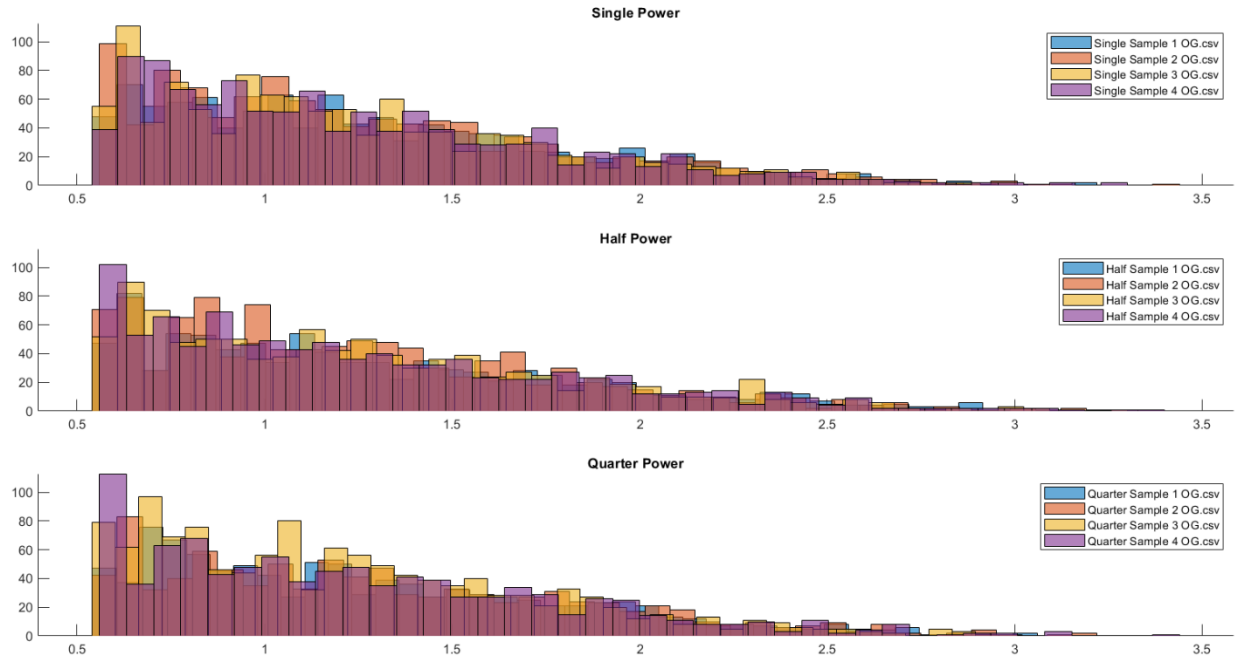

Figure 23: Log grain equivalent circle diameter normalized histograms by thermal history category.

Next, a Kolmogorov–Smirnov (K-S) test was performed to determine whether all of the replicates for each thermal history category could be combined into one corresponding dataset per category for both grain area and equivalent circle diameter. The K-S test serves as a nonparametric evaluation of the equality of continuous, one-dimensional probability distributions that can be used to compare two or more samples. The K-S tests (total of 36) for each thermal history category for both grain area and equivalent circle diameter determined that all replicates can be combined and treated as one overarching parameter set.

For additional data distribution visualization and an opportunity to determine significant difference in means by inspection, normalized box and whisker plots were created for both the grain area (Figure 24) and grain equivalent circle diameter (Figure 25) data across each thermal history category with combined replicate data.

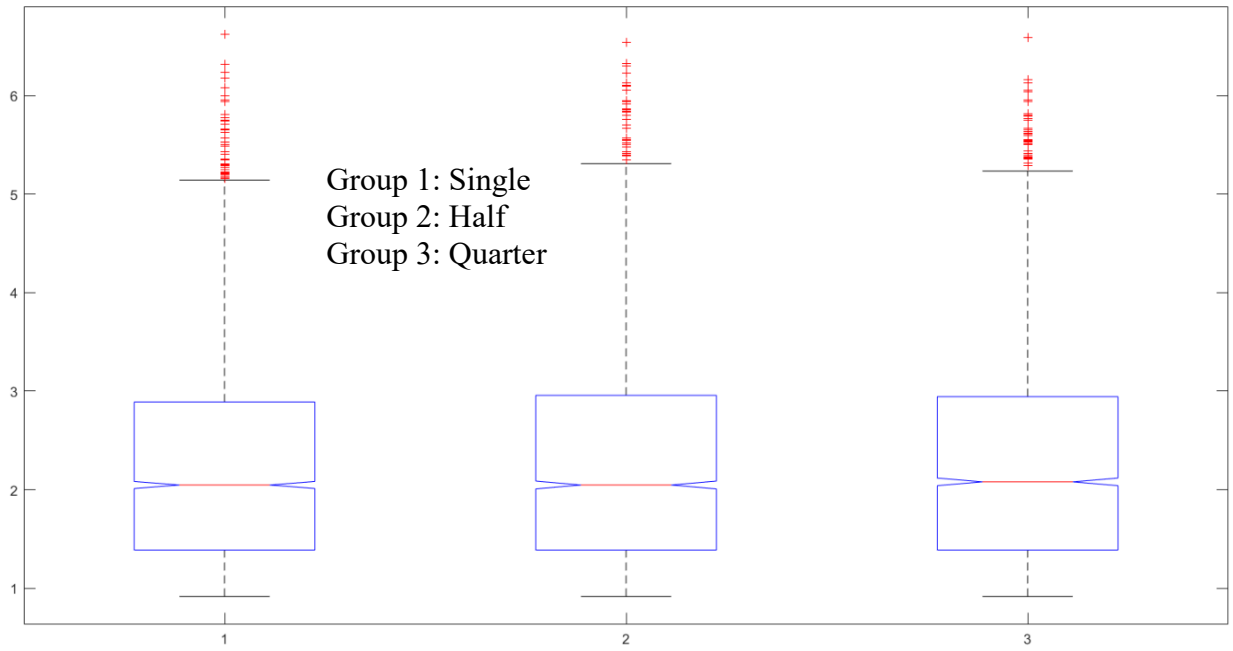

Figure 24: Log grain area normalized box & whisker plot by thermal history category with combined replicate data. Left (Group 1) is the normalized box and whisker plot for the grain area of the standard thermal history builds, middle (Group 2) is for the mixed alternating standard and half power exposure samples, and right (Group 3) is for the mixed alternating standard and quarter power exposure samples.

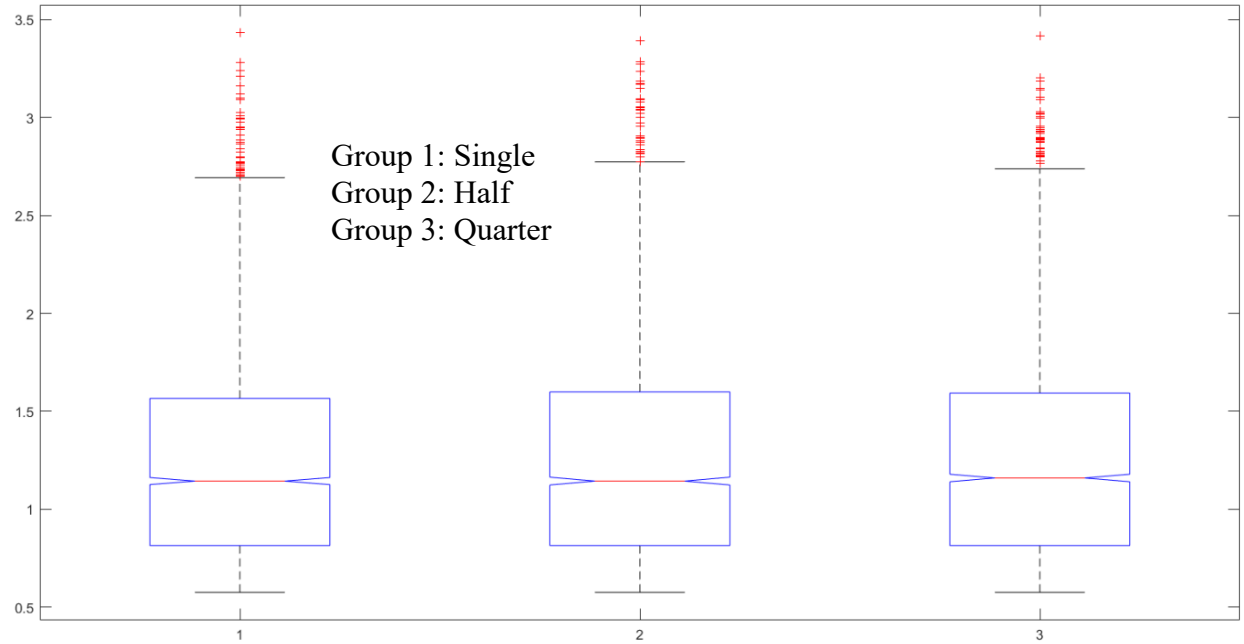

Figure 25: Log grain equivalent circle diameter normalized box & whisker plot by thermal history category with combined replicate data. Left (Group 1) is the normalized box and whisker plot for the grain equivalent circle diameter of the standard thermal history builds, middle (Group 2) is for the mixed alternating standard and half power exposure samples, and right (Group 3) is for the mixed alternating standard and quarter power exposure samples.

Finally, analysis of variance (ANOVA) was used to test for differences between two or more means by thermal history category. All six ANOVAs (three for grain area and three for grain equivalent circle diameter) resulted in no statistically significant difference between means across thermal history categories. Therefore, no quantitative difference in resulting microstructure across thermal history categories was discovered with EBSD analysis.

Conclusions

This research suggests that an ex-situ H900 heat treatment is effective in eliminating microstructural and mechanical property differences between 17-4PH stainless steel samples produced with drastically varied L-PBF AM thermal histories. Standard quasi-static tensile testing results revealed no statistically significant differences in global mechanical response through yield strength, ultimate strength, or elongation at break across the five thermal history categories for each thickness subset (2mm and 6mm) of specimens. Additionally, no significant differences in local mechanical response as examined by microhardness mapping were observed. Qualitative metallography indicated ductile fracture across all tensile specimens, and no discernable differences in microstructural features such as matrix phase or precipitation features were observed with optical or SEM techniques. Similarly, EBSD measurements revealed no statistically significant differences in microstructure between samples as identified by grain areas, grain equivalent circle diameters, or metallurgical phase fractions. The results of this research are encouraging when considering the possibility of extrapolation to homogenizing any differences in microstructure and mechanical properties of other metallic alloys produced by AM processes with inherent thermal history differences by implementation of ex-situ heat treatments. However, because no analysis was performed on as-built specimens prior to heat treating, it is currently impossible to conclude whether the results are due to an effective heat treatment or ineffective processing parameters.

To further investigate potential differences in local versus global mechanical response and corresponding microstructure, several characterization techniques are proposed for future work. Using digital image correlation (DIC) during tensile testing could help examine localized strain behaviors. For local microstructural differences, using an EBSD map that stitches several scan areas would help to identify phases and grain sizes and morphologies, and electron probe microanalysis (EPMA) could be used to detect any potential differences in chemical composition due to loss of certain alloying elements during solidification. Energy dispersive x-ray spectroscopy can be used to map the compositions of the various precipitates that form at different scales during the solidification and heat treatment of this alloy. Additionally, it would be valuable to use a design of experiments to examine the effects of scan patterns, build plate layout, and tool paths on the localized mechanical response and microstructure. Finally, all of the work already completed here and proposed for future study of these H900 parts should be replicated on the as-built versions of these samples to see what the pre-heat treatment mechanical response and microstructure would be both locally and globally to get a full understanding of how intentionally manipulating thermal histories affects L-PBF AM 17-4PH parts.

Disclaimer

This material is based on work funded by the Defense Threat Reduction Agency (DTRA) through the Naval Sea Systems Command (NAVSEA) under Contract No. N000024-18-F-6401, Delivery Order 21F8353. The opinions, findings, conclusions, and recommendations expressed in this material are those of the authors and do not necessarily reflect the views of NAVSEA, nor do they reflect the views of DTRA or collaborators at NAVSEA. Additional funding for this work was provided by the Materials Research Institute (MRI) at Penn State's Seed Grant 2020 program.

Acknowledgments

The authors would like to thank Dr. Ken Meinert and Mr. Corey Dickman from the Center for Innovative Materials Processing through Direct Digital Deposition (CIMP-3D) at Penn State for performing the powder distribution analysis and assistance with building the metal samples used in this study, respectively, as well as Mr. Eric Strauch of the Applied Research Laboratory (ARL) at Penn State for performing the tensile testing of the specimens. An additional acknowledgment is due to CIMP-3D for allowing access to their metallographic laboratory for sample preparation and the Materials Characterization Laboratory (MCL) at Penn State for equipment time on the vibratory polisher and FESEM for EBSD measurements. Finally, the support from Solar Atmospheres in Hermitage, PA with heat treating the samples and Acura-Cut in Pleasant Gap, PA for wire EDM services is greatly appreciated.

References

[1] I. Gibson, D. Rosen, and B. Stucker, *Additive Manufacturing Technologies*, 2nd ed. New York, NY: Springer, 2015.

[2] J. O. Milewski, *Additive Manufacturing of Metals*. Springer International Publishing, 2017. doi: 10.1007/978-3-319-58205-4.

[3] T. DebRoy *et al.*, "Additive manufacturing of metallic components – Process, structure and properties," *Prog. Mater. Sci.*, vol. 92, pp. 112–224, Mar. 2018, doi: 10.1016/j.pmatsci.2017.10.001.

[4] S. S. Al-Bermani, "An Investigation into Microstructure and Microstructural Control of Additive Layer Manufactured Ti-6Al-4V by Electron Beam Melting," Ph.D. Dissertation, University of Sheffield, Sheffield, South Yorkshire, England, 2011. [Online]. Available: https://etheses.whiterose.ac.uk/14694/

[5] W. E. Frazier, "Metal Additive Manufacturing: A Review," *J. Mater. Eng. Perform.*, vol. 23, no. 6, pp. 1917–1928, 2014.

[6] S. Cheruvathur, E. A. Lass, and C. E. Campbell, "Additive Manufacturing of 17-4 PH Stainless Steel: Post-processing Heat Treatment to Achieve Uniform Reproducible Microstructure," *JOM*, vol. 68, no. 3, pp. 930–942, Mar. 2016, doi: 10.1007/s11837-015-1754-4.

[7] L. Carneiro, B. Jalalahmadi, A. Ashtekar, and Y. Jiang, "Cyclic deformation and fatigue behavior of additively manufactured 17–4 PH stainless steel," *Int. J. Fatigue*, vol. 123, pp. 22–30, Jun. 2019, doi: 10.1016/j.ijfatigue.2019.02.006.

[8] E. A. Lass, M. R. Stoudt, and M. E. Williams, “Additively Manufactured Nitrogen-Atomized 17-4 PH Stainless Steel with Mechanical Properties Comparable to Wrought,” *Metall. Mater. Trans. A*, vol. 50, no. 4, pp. 1619–1624, Apr. 2019, doi: 10.1007/s11661-019-05124-0.
[9] Y. Sun, R. J. Hebert, and M. Aindow, “Effect of heat treatments on microstructural evolution of additively manufactured and wrought 17-4PH stainless steel,” *Mater. Des.*, vol. 156, pp. 429–440, Oct. 2018, doi: 10.1016/j.matdes.2018.07.015.
[10] T. K. Shoemaker, Z. D. Harris, and J. T. Burns, “Comparing Stress Corrosion Cracking Behavior of Additively Manufactured and Wrought 17-4PH Stainless Steel,” *Corrosion*, vol. 78, no. 6, pp. 528–546, Apr. 2022, doi: 10.5006/4064.
[11] J. Schmelzle, E. V. Kline, C. J. Dickman, E. W. Reutzel, G. Jones, and T. W. Simpson, “(Re)Designing for Part Consolidation: Understanding the Challenges of Metal Additive Manufacturing,” *J. Mech. Des.*, vol. 137, no. 111404, Oct. 2015, doi: 10.1115/1.4031156.
[12] C. Fox, C. Tilton, C.-E. Rousseau, A. Shukla, C. Sheeley, and R. Hebert, “Dynamic Constitutive Behavior of Additively Manufactured 17-4PH Stainless Steel,” *J. Dyn. Behav. Mater.*, vol. 8, no. 2, pp. 242–254, Jun. 2022, doi: 10.1007/s40870-022-00328-9.
[13] B. McWilliams, B. Pramanik, A. Kudzal, and J. Taggart-Scarff, “High strain rate compressive deformation behavior of an additively manufactured stainless steel,” *Addit. Manuf.*, vol. 24, pp. 432–439, Dec. 2018, doi: 10.1016/j.addma.2018.09.016.
[14] Y. Sun, M. Aindow, and R. J. Hebert, “Effect of Part Placement Strategy on the Microstructure of Additively Manufactured 17-4PH Stainless Steel Thin-Wall Parts,” *Microsc. Microanal.*, vol. 25, no. S2, pp. 2572–2573, Aug. 2019, doi: 10.1017/S143192761901359X.
[15] Y. Sun, R. J. Hebert, and M. Aindow, “Effect of laser scan length on the microstructure of additively manufactured 17-4PH stainless steel thin-walled parts,” *Addit. Manuf.*, vol. 35, p. 101302, Oct. 2020, doi: 10.1016/j.addma.2020.101302.
[16] A. Soltani-Tehrani, J. Pegues, and N. Shamsaei, “Fatigue behavior of additively manufactured 17-4 PH stainless steel: The effects of part location and powder re-use,” *Addit. Manuf.*, vol. 36, p. 101398, Dec. 2020, doi: 10.1016/j.addma.2020.101398.
[17] A. Yadollahi, N. Shamsaei, S. M. Thompson, A. Elwany, and L. Bian, “Effects of building orientation and heat treatment on fatigue behavior of selective laser melted 17-4 PH stainless steel,” *Fatigue Fract. Behav. Addit. Manuf. Parts*, vol. 94, pp. 218–235, Jan. 2017, doi: 10.1016/j.ijfatigue.2016.03.014.
[18] A. Kudzal *et al.*, “Effect of scan pattern on the microstructure and mechanical properties of Powder Bed Fusion additive manufactured 17-4 stainless steel,” *Mater. Des.*, vol. 133, pp. 205–215, Nov. 2017, doi: 10.1016/j.matdes.2017.07.047.
[19] P. Leo, M. Cabibbo, A. Del Prete, S. Giganto, S. Martínez-Pellitero, and J. Barreiro, “Laser Defocusing Effect on the Microstructure and Defects of 17-4PH Parts Additively Manufactured by SLM at a Low Energy Input,” *Metals*, vol. 11, no. 4, 2021, doi: 10.3390/met11040588.
[20] R. Johnson, I. S. Grech, N. Wint, and N. P. Lavery, “Effect of Build Bed Location on Density and Corrosion Properties of Additively Manufactured 17-4PH Stainless Steel,” in *Sustainable Design and Manufacturing 2020*, S. G. Scholz, R. J. Howlett, and R. Setchi, Eds., Singapore: Springer Singapore, 2021, pp. 425–438.
[21] J. Sripada *et al.*, “Effect of hot isostatic pressing on microstructural and micromechanical properties of additively manufactured 17–4PH steel,” *Mater. Charact.*, vol. 192, p. 112174, Oct. 2022, doi: 10.1016/j.matchar.2022.112174.

[22] A. Pellegrini, F. Lavecchia, M. G. Guerra, and L. M. Galantucci, "Influence of aging treatments on 17–4 PH stainless steel parts realized using material extrusion additive manufacturing technologies," *Int. J. Adv. Manuf. Technol.*, vol. 126, no. 1, pp. 163–178, May 2023, doi: 10.1007/s00170-023-11136-3.
[23] S. D. Meredith, J. S. Zuback, J. S. Keist, and T. A. Palmer, "Impact of composition on the heat treatment response of additively manufactured 17–4 PH grade stainless steel," *Mater. Sci. Eng. A*, vol. 738, pp. 44–56, Dec. 2018, doi: 10.1016/j.msea.2018.09.066.
[24] E. A. Lass, F. Zhang, and C. E. Campbell, "Nitrogen Effects in Additively Manufactured Martensitic Stainless Steels: Conventional Thermal Processing and Comparison with Wrought," *Metall. Mater. Trans. A*, vol. 51, no. 5, pp. 2318–2332, May 2020, doi: 10.1007/s11661-020-05703-6.
[25] L. Li, "Heat Treating of Precipitation-Hardenable Stainless Steels and Iron-Base Superalloys," in *Heat Treating of Irons and Steels*, J. Dossett and G. E. Totten, Eds., in ASM Handbook, no. Heat Treating, vol. 4D. Materials Park, OH: ASM International, 2014, pp. 1–21. [Online]. Available: https://doi.org/10.31399/asm.hb.v04d.a0005961
[26] "ASTM Standard A564/A564M: Standard Specification for Hot-Rolled and Cold-Finished Age-Hardening Stainless Steel Bars and Shapes." ASTM International, 2017. [Online]. Available: https://doi.org/10.1520/A0564_A0564M-13
[27] V. Herrera Lara, L. Guerra Fuentes, O. Covarrubias Alvarado, A. Salinas Rodriguez, and E. Garcia Sanchez, "Hot Ductility of the 17-4 PH Stainless Steels," *J. Mater. Eng. Perform.*, vol. 25, no. 3, pp. 1041–1046, Mar. 2016, doi: 10.1007/s11665-016-1895-9.
[28] J. R. Davis, Ed., "Heat Treating of Stainless Steels and Heat-Resistant Alloys," in *Metals Handbook Desk Edition*, 2nd Ed.Materials Park, OH: ASM International, 1998, pp. 1025–1030. doi: 10.31399/asm.hb.mhde2.a0003203.
[29] "ASTM Standard E8/E8M: Standard Test Methods for Tension Testing of Metallic Materials." ASTM International, 2022. [Online]. Available: https://doi.org/10.1520/E0008_E0008M-22
[30] "Additive Manufacturing Powders Specification Guide." Powder Alloy Corporation, 2019. [Online]. Available: https://powderalloy.com/wp-content/uploads/2020/04/PAC-Linecard-420-1.pdf
[31] "ASTM Standard B214: Standard Test Method for Sieve Analysis of Metal Powders." ASTM International, 2020. [Online]. Available: https://doi.org/10.1520/B0214-22
[32] "ASTM Standard B822: Standard Test Method for Particle Size Distribution of Metal Powders and Related Compounds by Light Scattering." ASTM International, 2020. [Online]. Available: https://doi.org/10.1520/B0822-20
[33] "ASTM Standard B213: Standard Test Methods for Flow Rate of Metal Powders Using the Hall Flowmeter Funnel." ASTM International, 2020. [Online]. Available: https://doi.org/10.1520/B0213-20
[34] "ASTM Standard F3301: Standard for Additive Manufacturing – Post Processing Methods – Standard Specification for Thermal Post-Processing Metal Parts Made Via Powder Bed Fusion." ASTM International, 2018. [Online]. Available: https://doi.org/10.1520/F3301-18A
[35] "ASTM Standard E3: Standard Guide for Preparation of Metallographic Specimens." ASTM International, 2017. [Online]. Available: https://doi.org/10.1520/E0003-11R17

[36] “ASTM Standard E92: Standard Test Methods for Vickers Hardness and Knoop Hardness of Metallic Materials.” ASTM International, 2017. [Online]. Available: https://doi.org/10.1520/E0092-17